remote sensing

MDPI

Article

Early Mission Calibration Performance of NOAA-21 VIIRS Reflective Solar Bands

Ning Lei [1,*], Xiaoxiong Xiong [2], Kevin Twedt [1], Sherry Li [1], Tiejun Chang [1], Qiaozhen Mu [1] and Amit Angal [1]

[1] Science Systems and Applications, Inc., 10210 Greenbelt Road, Lanham, MD 20706, USA; kevin.twedt@ssaihq.com (K.T.); xuexia.chen@ssaihq.com (S.L.); tiejun.chang@ssaihq.com (T.C.); qiaozhen.mu@ssaihq.com (Q.M.); amit.angal@ssaihq.com (A.A.)
[2] NASA Goddard Space Flight Center, Greenbelt, MD 20771, USA; xiaoxiong.xiong-1@nasa.gov
* Correspondence: ning.lei@ssaihq.com

Abstract: The Visible Infrared Imaging Radiometer Suite (VIIRS) is one of the key instruments on the recently launched NOAA-21 (previously known as JPSS-2) satellite. The VIIRS, like its predecessors on the SNPP and NOAA-20 satellites, provides daily global coverage in 22 spectral bands from 412 nm to 12 µm. The geometrically and radiometrically calibrated observations are the basis for many operational applications and scientific research studies. A total of 14 of the 22 bands are reflective solar bands (RSBs), covering photon wavelengths from 412 nm to 2.25 µm. The RSBs were radiometrically calibrated prelaunch and have been regularly calibrated on orbit through the onboard solar diffuser (SD) and scheduled lunar observations. The on-orbit SD's reflectance change is determined by the onboard solar diffuser stability monitor (SDSM). We review the calibration algorithms and present the early mission performance of the NASA N21 VIIRS RSBs. Using the calibration data collected at both the yaw maneuver and regular times, we derive the screen transmittance functions. The visible and near-infrared bands' radiometric gains have been stable, nearly independent of time, and so were the radiometric gains of the shortwave-infrared bands after the second mid-mission outgassing. Further, we assess the Earth-view striping observed in the immediate prior collection (Collection 2.0) and apply a previously developed algorithm to mitigate the striping. The N21 VIIRS RSB detector signal-to-noise ratios are all above the design values with large margins. Finally, the uncertainties of the retrieved Earth-view top-of-the-atmosphere spectral reflectance factors at the respective typical spectral radiance levels are estimated to be less than 1.5% for all the RSBs, except band M11 whose reflectance factor uncertainty is 2.2%.

Keywords: VIIRS; JPSS; SNPP; reflective solar bands; calibration; performance; algorithms; uncertainty; screen transmittance

Citation: Lei, N.; Xiong, X.; Twedt, K.; Li, S.; Chang, T.; Mu, Q.; Angal, A. Early Mission Calibration Performance of NOAA-21 VIIRS Reflective Solar Bands. *Remote Sens.* **2024**, *16*, 3557. https://doi.org/10.3390/rs16193557

Academic Editor: Carmine Serio

Received: 29 July 2024
Revised: 18 September 2024
Accepted: 20 September 2024
Published: 24 September 2024

1. Introduction

The Visible Infrared Imaging Radiometer Suite (VIIRS) is a key instrument on the Suomi National Polar-orbiting Partnership (SNPP) satellite and the Joint Polar Satellite System (JPSS). The most recent VIIRS instrument is aboard the pseudo-Sun synchronous JPSS-2 satellite—launched on 10 November 2022—which was renamed as the NOAA-21 (N21) satellite after the satellite launch. The N21 satellite has a nominal local equator crossing time of 13:30 in ascending node and is maintained at an average altitude of 839 km [1,2]. VIIRS is a whiskbroom scanning radiometer, providing daily global coverage in 22 spectral bands [3–5]. The data collected by VIIRS are the basis for nearly 30 imagery and geophysical parameters for research studies and weather forecasting [6,7]. The N21 VIIRS is the third VIIRS instrument, following the previous two on the SNPP and NOAA-20 (N20) satellites launched on 28 October 2011 and 18 November 2017, respectively.

The 22 VIIRS bands consist of 14 reflective solar bands (RSBs), detecting photons in the wavelength range of 412 nm to 2.25 µm; 7 thermal emissive bands, detecting photons in the range of 3.7 to 12.0 µm; and a panchromatic day–night band which has multiple gain stages

to achieve a large dynamic range. Within the 14 RSBs, there are 3 imaging and 11 moderate spatial resolution bands (I- and M-bands) with nominal pixel sizes on the Earth surface at nadir of 375 by 375 and 750 by 750 m^2, respectively. Each M- and I-band consists of 16 and 32 detectors, respectively. Six of the 11 M-bands are dual-gain, and the three I-bands are single gain. The spectral design specifications for the 14 RSBs are listed in Table 1.

Table 1. Design parameters for the VIIRS RSB band center wavelengths, band passes, SNRs, and typical, minimum, and maximum scene spectral radiances in $Wm^{-2}SR^{-1}\mu m^{-1}$. HG refers to the high-gain stage, and LG refers to the low-gain stage.

Band	Center Wavelength (nm)	Bandwidth (nm)	SNR Spec	Lmin	Ltyp	Lmax
I1	640	80	119	5	22	718
I2	865	39	150	10.3	25	349
I3	1610	60	6	1.2	7.3	72.5
M1HG	412	20	352	30	44.9	135
M1LG			316	135	155	615
M2HG	445	18	380	26	40	127
M2LG			409	127	146	687
M3HG	488	20	416	22	32	107
M3LG			414	107	123	702
M4HG	555	20	362	12	21	78
M4LG			315	78	90	667
M5HG	672	20	242	8.6	10	59
M5LG			360	59	68	651
M6	746	15	199	5.3	9.6	41
M7HG	885	39	215	3.4	6.4	29
M7LG			340	29	33.4	349
M8	1240	20	74	3.5	5.4	164.9
M9	1378	15	83	0.6	6	77.1
M10	1610	60	342	1.2	7.3	71.2
M11	2250	50	90	0.12	1.0	31.8

The VIIRS RSBs were radiometrically calibrated prelaunch [8–10]. However, once on orbit, the RSB radiometric performance may change, as observed in previous VIIRS instruments [11–15]. VIIRS is equipped with onboard calibrators to perform on-orbit radiometric calibration. For the RSBs, the onboard solar diffuser (SD), when fully solar illuminated, provides a known radiance source (by design) for the calibration. The SD's bidirectional reflectance distribution function (BRDF) changes its value on orbit because of solar exposure, perhaps coupled with SD surface contamination [16]. VIIRS is equipped with a solar diffuser stability monitor (SDSM) to track the SD's BRDF on-orbit change by comparing the SDSM detector signal strengths when viewing the SD surface and the Sun at almost the same time. SDSM detectors 1 to 7 spectrally match bands M1–M7, and SDSM detector 8 centers at 926 nm by design. The relative positions of the VIIRS calibrators, including the space view (SV) port through which a background digital number (DN) is read for the RSBs, along with the major optical components, are shown in Figure 1.

The solar illumination of the SD is through holes in an opaque plate, denoted as the SD screen. The eight SDSM detectors observe the Sun through another opaque plate with holes, denoted as the SDSM screen. Figure 2 shows a schematic of the VIIRS RSB on-orbit radiometric calibration. The SDSM receives the SD-scattered sunlight in a slightly backward direction whereas the SD-scattered sunlight received by the RSB detectors through the rotating telescope assembly (RTA) is in a forward direction. For the two observations, the amounts of the SD BRDF on-orbit changes may not be the same. In fact, it has been shown

that the BRDF on-orbit changes are angle-dependent at the shorter-wavelength region of the VIIRS RSBs [17–20]. This paper shows how we handle this issue for the N21 VIIRS SD.

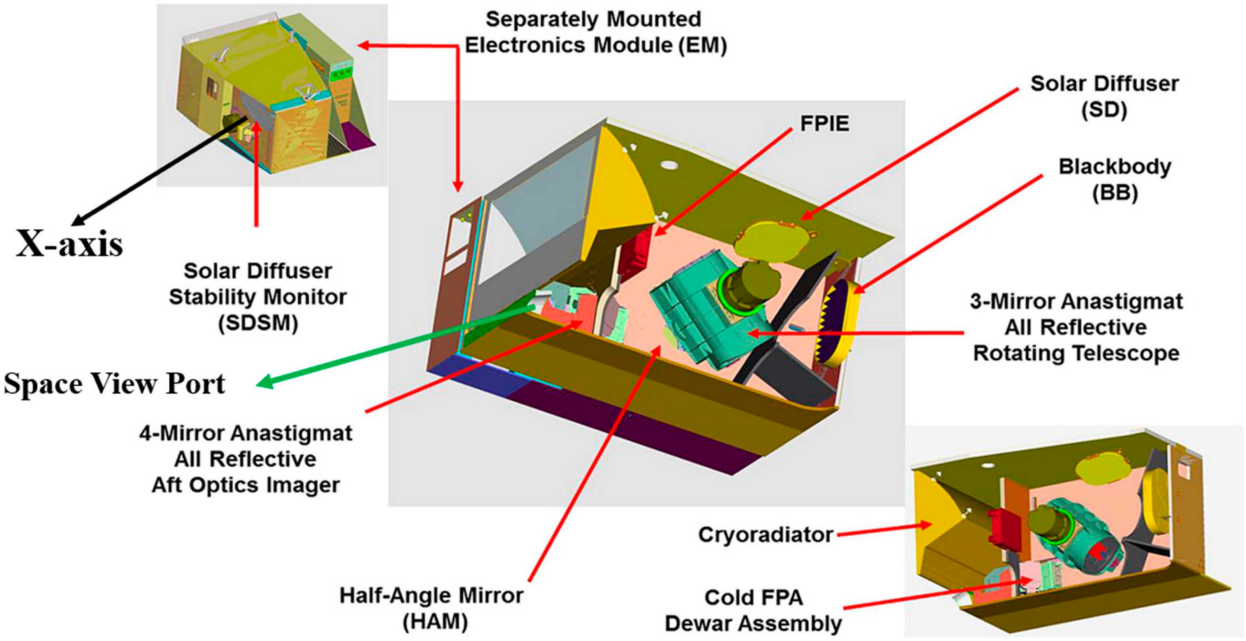

Figure 1. Major physical components and their relative positions of the VIIRS instrument, including the on-orbit calibrators.

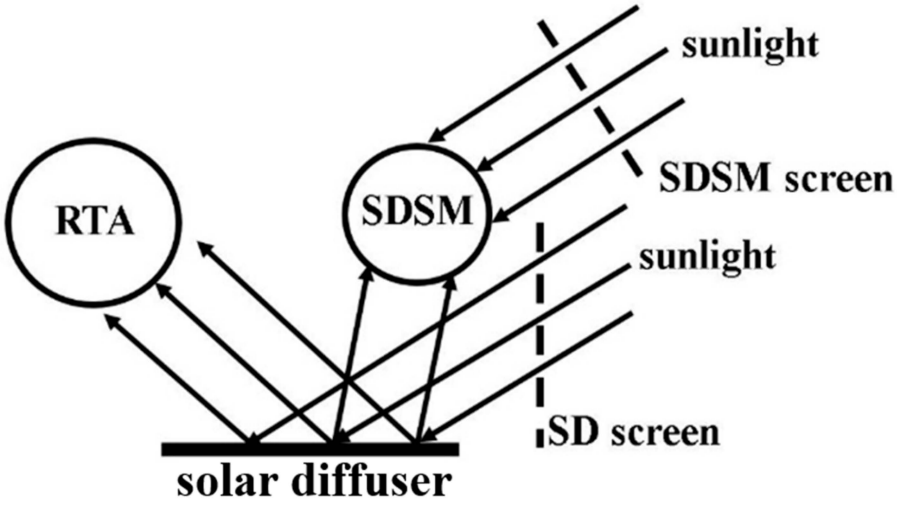

Figure 2. A schematic of the VIIRS RSB on-orbit radiometric calibration. RTA refers to the telescope (rotating telescope assembly), SD refers to the solar diffuser, and SDSM refers to the solar diffuser stability monitor.

The N21 VIIRS SD and SDSM screen transmittances were measured prelaunch [21,22]. However, these prelaunch transmittances are not accurate enough, causing large unexpected undulations in the retrieved SD BRDF on-orbit change factor and, as a result, in the retrieved RSB detector radiometric gains. The screen function inaccuracy is probably partly due to how accurately the screens were mounted on the VIIRS. To refine the transmittances, as for the SNPP and N20 VIIRS [23,24], N21 performed yaw maneuvers on satellite orbits 1649 to 1663. We used the calibration data collected on the yaw maneuver orbits to refine the transmittances [25]. The yaw maneuvers, however, have large gaps in the solar azimuth angle so that the derived screen transmittance functions, especially the SDSM screen transmittance function, are still not accurate enough. Consequently, the retrieved

SDSM SD BRDF on-orbit change factors still have large, unexpected undulations across the time domain, indicating that the SDSM-related screen functions are still not accurate enough. This was also the case for the SNPP and N20 VIIRS when only the data on the yaw maneuver orbits were used to derive the screen functions. To resolve the issue for the SNPP VIIRS, we developed a methodology to further refine the screen transmittances by adding some regular calibration data [26,27]. We also successfully applied this methodology to the N20 VIIRS [28]. Here, we apply the methodology to refine the N21 VIIRS screen transmittance functions, with a slight improvement that addresses the adverse impact of the SDSM detector gain change correlated to the temperature change for the eight SDSM detectors.

In the early days of the mission, the N21 VIIRS shortwave-infrared (SWIR) bands experienced rapid gain degradation. The root cause may be ice accumulated on the dewar walls of the detector focal plane. To remove the ice, mid-mission outgassing was performed twice. Along with the outgassing events, other major events that impacted the N21 VIIRS radiometric performance are listed in Table 2.

Table 2. Major N21 VIIRS events.

Description	Mission Day	Orbit	Start Date/Time	End Date/Time
Launch	001	-	10 November 2022_09:49z	Lift off 1:49 PST/4:49 EST
SDSM first measurement, 5 min every orbit (started 3 min too early)	011	149	20 November 2022	-
SDSM timing corrected by extending measurement from 5 to 8 min	012	160	21 November 2022	-
SDSM measurement reduced back to 5 min	022	307	1 December 2022	
Nadir aperture door open	026	360	5 December 2022_17:37z	-
SDSM operation change to once every other orbit	029	405	8 December 2022	
N21 Ka-band transmitter (KaTX-1) anomaly	037	508	16 December 2022_02:49z	-
N21 Ka-band transmitter #2 (KaTX-2) activated after 48 days	085		2 February 2023_15:22:52z	
Cryoradiator cooler door open	091		8 February 2023_15:46z	-
Cold focal plane assembly CFPA) (stable)	093		-	10 February 2023_02:30z
SDSM operation change to once daily (36 cycles)	097		14 February 2023	
Mid-mission outgassing	106–108	1485–1519	23 February /2023_14:25:42z	25 February 2023_08:45:03z
CFPA return to nominal 82K (stable)	109	1528	-	26 February /2023_01:10z
CFPA change from 82K to 80K (only LWIR heater controls both CFPAs)	114	1610–1611	3 March 2023_19:33:23z	3 March 2023_20:29:20z
Yaw maneuvers 14 orbits yaw + 1 middle orbit, no yaw; SDSM, 5 min	117	1649–1663	6 March 2023_13:22:30z	7 March 2023_13:14:33z

Table 2. *Cont.*

Description	Mission Day	Orbit	Start Date/Time	End Date/Time
Pitch maneuver (deep space view)	121	1705	10 March 2023_11:37:05z	10 March /2023_12:10:51z
CFPA return to nominal 80K stable	121	1711	-	10 March 2023_22:42z
Mid-mission outgassing #2	474–476	6715–6743	26 February 2024_15:05:21z	28 February 2024_13:57:45z
VIIRS in active mode	475	6733	27 february 2024_21:00:00z	-
CFPA return to nominal 80K stable	477	6753	-	29 February 2024_07:30z

Since the N21 VIIRS started collecting Earth data, the NASA VIIRS Characterization Support Team has delivered calibration lookup tables (LUTs) that are used to generate Earth-view spectral radiance and reflectance. Since the satellite launch, three versions of the LUTs have been delivered with successive improvements. In Table 3, we list the collections and the associated calibration algorithms.

Table 3. NASA Level 1B product collections for the N21 VIIRS and the corresponding RSB calibration algorithms. AS: archive set. Collection 1.0 does not have an AS number because it is for internal testing only and is not publicly released. Collection 2.1 is undergoing testing as of this writing but is expected to be released soon under AS 5201.

Collections/AS #s	RSB Calibration Algorithms
1.0	Screen functions from the yaw maneuvers, Thuillier solar spectral power, $H_{RTA} = H^{M}_{SDSM}$, H_{RTA}(SWIR) = 1
2.0/5200c	Screen functions from the yaw maneuvers, Thuillier solar spectral power, SDSM-measured H-factor without RSR deconvolution and a multiplicative factor that is the mean of F(H_{RTA}; SNPP)/F(H^{M}_{SDSM}, SNPP) and F(H_{RTA}; N20)/F(H^{M}_{SDSM}, N20), $\tau_{SD}BRDF_{RTA}$(M11) is 1.061 of the prelaunch value
2.1/5201	Screen functions from both the yaw maneuver and a small portion of regular times, TSIS-1 solar spectral power, SDSM-measured H-factor without RSR deconvolution and a multiplicative factor that is F(H_{RTA}; SNPP)/F(H^{M}_{SDSM}, SNPP), wavelength power law for H^{M}_{SDSM} at the SWIR wavelengths, H_{RTA}(SWIR)= H^{M}_{SDSM}(SWIR), $\tau_{SD}BRDF_{RTA}$(M11) is 1.061 of the prelaunch value, M4 low-gain c-coefficients updated, VisNIR band striping mitigated

This paper reviews the N21 VIIRS RSB calibration algorithms and shows the results. As of this writing, the current version of NASA's Level 1B products (L1B)— geometrically and radiometrically calibrated spectral reflectance and radiance—for the N21 VIIRS is Collection 2.0 (C2.0). An improved version, Collection 2.1 (C2.1), is currently in testing and will be released soon (see Table 3). Unless otherwise stated, the calibration algorithms and results discussed here are for the C2.1 version. In addition, we assessed the striping from the retrieved top-of-the-atmosphere spectral reflectance in Collection 2.0 and applied a methodology developed previously to mitigate the striping. We also estimated the uncertainties of the retrieved top-of-the-atmosphere spectral reflectance factor.

Throughout this paper, we have used acronyms to simplify the writing, especially within equations. To facilitate reading this paper, we have listed the acronyms and their definitions in Table A1 in Appendix B.

2. Radiometric Calibration Methodology

The N21 VIIRS RSB on-orbit radiometric calibration algorithms mainly follow those used by the SNPP and N20 VIIRS instruments [5,12,16,29–31]. The scene spectral radiance retrieved by a VIIRS RSB detector, weighted by the detector's spectral response, $\overline{L}$ (the bar on top of the spectral radiance symbol, L, indicates the spectral-response-weighted average) is calculated through a quadratic polynomial of its background subtracted digital number, dn.

$$\overline{L} = \frac{F\sum_{i=0}^{2} c_i dn^i}{RVS(\lambda_B, \theta_S)}, \quad (1)$$

where F is a correction factor to the summation, the so-called F-factor [5], $\{c_i; i = 0, 1, 2\}$ is determined prelaunch, RVS (response versus scan angle) is the half-angle mirror's (HAM's) reflectivity relative to its value when the RTA views the SV port center, λ_B is the band center wavelength, and θ_S is the RTA scan angle. Equation (1) needs to be accurate between the minimum and maximum spectral radiances, L_{min} and L_{max} (see Table 1). The F-factor and the c-coefficients depend on the focal plane and electronics temperatures, the electronics side, band, detector, detector gain stage, and the HAM side.

The VIIRS HAM is behind the RTA's four reflective mirrors in the optical path so that the HAM's surface is shielded from large solar bombardment. As a result, we expect the RVS to be stable on orbit. Indeed, we have not found that the RVS has changed on orbit for the SNPP VIIRS HAM [32]. Hence, our efforts in the VIIRS RSB on-orbit radiometric calibration focuses on calculating the F-factor.

We retrieve the F-factor using the sunlight scattered by the SD when it is fully solar illuminated. The solar angular range over which the SD is fully illuminated as viewed by the VIIRS RSB and SDSM detectors is called the calibration sweet spot. When fully illuminated, at a given wavelength λ and time t from the start of the mission, the spectral radiance provided by the SD at the RSB detector SD view direction is given by

$$L_{SD}(\lambda, t) = \frac{\Phi_{SUN}(\lambda, t)}{4\pi d^2_{VIIRS-SUN}} \times \tau_{SD} BRDF_{RTA}\left(\lambda, t = 0, \vec{\phi}\right) H_{RTA}\left(\lambda, t, \vec{\phi}\right) \sin\phi_{V,SD}, \quad (2)$$

where Φ_{SUN} is the solar spectral power; $d_{VIIRS-SUN}$ is the VIIRS-Sun distance; τ_{SD} is the SD screen transmittance, which is approximately 11% across the sweet spot angles [21,22]; $BRDF_{RTA}$ refers to the BRDF at the RTA SD view direction; the "0" inside the brackets of $BRDF_{RTA}$ refers to the mission's starting time; and $\vec{\phi}$ is the solar angle, which is an angle that the solar vector makes with respect to a reference system. τ_{SD} and $BRDF_{RTA}\left(\lambda, t = 0, \vec{\phi}\right)$ were measured prelaunch at six wavelengths from 422 nm to 1.626 mm [33]. In Equation (2), H_{RTA} is the $BRDF_{RTA}$ on-orbit change factor, the so-called H-factor, at the RTA SD view direction, and $\phi_{V,SD}$ is the angle between the solar vector and the SD surface plane.

A VIIRS RSB detector can sense a photon over a spectrum of wavelengths, quantified by its relative spectral response function (RSR) which is typically defined as the spectral response function divided by its maximum value across the wavelengths. As a result, when the detector receives the SD-scattered sunlight, the detector's digital response, dn_{SD}, relates to L_{SD} as

$$F\sum_{i=0}^{2} c_i dn^i_{SD} = \frac{RVS(\lambda_B, \theta_S)\int_0^\infty RSR \times L_{SD}(\lambda, t) d\lambda}{\int_0^\infty RSR \times d\lambda}, \quad (3)$$

From Equation (3), we retrieve the F-factor.

The right side of Equation (3) is just the RVS multiplied by the RSR weight-averaged spectral radiance from the SD, namely, $\overline{L_{SD}}(\lambda_B, t)$. Retrieving the F-factor from the sunlit SD relies on knowing how much the SD's BRDF changes over the course of the mission. Because of the angular dependence of the H-factor [18–20], we face a challenge in finding the H-factor for the RSB SD view, H_{RTA}, from the H-factor retrieved by the SDSM measurements which are for the SDSM SD view.

We calculate the SDSM directly measured H-factor for the SDSM SD view, $H^{\mathrm{M}}_{\mathrm{SDSM}}$, in the traditional way [5,16], comparing the SDSM detector Sun-view signal strength to that of the SD view:

$$H^{\mathrm{M}}_{\mathrm{SDSM}}(\lambda_d,\ t,\ \vec{\phi}(t)) = \frac{S_{\mathrm{H}} \times \frac{dc_{\mathrm{SD}}(t,\ d)}{dc_{\mathrm{SUN}}(t',\ d)} \times \frac{\tau^{\mathrm{R}}_{\mathrm{SDSM,eff}}\left(\vec{\phi}(t'),\ d\right)}{\tau^{\mathrm{R}}_{\mathrm{SD,eff}}\left(\vec{\phi}(t),\ d\right)}}{\mathrm{BRDF}_{\mathrm{SDSM}}\left(\lambda_d, 0, \vec{\phi}(t)\right)\sin\phi_{\mathrm{V,SD}}(t)}, \tag{4}$$

where the superscript "M" indicates the H-factor is the measured H-factor and may not be the same as the true H-factor for the SDSM SD view because of the impact of the SDSM detector RSR. In Equation (4), t is the time when the SDSM detector views the SD and t' is the time when the detector views the Sun. d in Equation (4) represents the SDSM detector index, S_{H} is a scale factor determined in such a way that $H^{\mathrm{M}}_{\mathrm{SDSM}}$ is unity at the start of the mission, dc_{SD} is the SDSM detector SD view digital count with the background subtracted, dc_{SUN} is the SDSM detector Sun-view digital count with the background subtracted, $\mathrm{BRDF}_{\mathrm{SDSM}}$ is the prelaunch-determined SD BRDF for the SDSM SD view, and $\tau^{\mathrm{R}}_{\mathrm{SD,eff}}$ and $\tau^{\mathrm{R}}_{\mathrm{SDSM,eff}}$ are the relative effective SD and SDSM screen transmittances.

To find H_{RTA} from $H^{\mathrm{M}}_{\mathrm{SDSM}}$, we typically rely on lunar observations [19,30] because the lunar solar reflectance is very stable over time [34]. Observation of the Moon is performed through the SV port, often requiring a roll rotation of the spacecraft. In a single RTA scan, the detector array of a VIIRS RSB can completely cover the lunar disk. Each lunar pixel contributes to the total lunar spectral irradiance at the VIIRS location. Hence, after adding the lunar spectral irradiance from all the lunar pixels, we find the total lunar spectral irradiance at the VIIRS location. Comparing with the known total lunar spectral irradiance at the VIIRS location, $\overline{I_{\mathrm{ROLO}}}$, given by the Robotic Lunar Observatory (ROLO) model developed by the US Geological Survey [35], up to a non-unity factor whose sources are not entirely known, we can retrieve the F-factor from the lunar view [36] through

$$F_{\mathrm{MOON}} = \frac{\overline{I_{\mathrm{ROLO}}}}{\sum_{\mathrm{pixel,scan}} \overline{L}_{\mathrm{MOON,PL,pixel,scan}} \cdot \Omega_B \cdot \frac{N_{\mathrm{agg}}}{N_{\mathrm{SCAN}}}}, \tag{5}$$

where Ω_{B} is the VIIRS RSB detector's field-of-view solid angle (for one frame of the scene) before aggregation, N_{agg} is the scan frame aggregation factor, N_{SCAN} is the number of scans that have the entire lunar disk captured by the detector array in a band, and $\overline{L}_{\mathrm{MOON,PL,pixel,scan}}$ is the spectral-response-function-weighted lunar spectral radiance per pixel for a given scan with the prelaunch c-coefficients. The reason for using N_{SCAN} scans is to reduce uncertainty in the calculated total lunar spectral irradiance by averaging. Because some pixels may be aggregated from two or three primary frames and Ω_{B} is the detector's field-of-view solid angle before aggregation, $N_{\mathrm{agg}}\Omega_B$ reflects the field-of-view solid angle for the two or three primary frames.

Because of the non-unity factor associated with F_{MOON}, we use F_{MOON} on a relative basis: We fit an F-factor model to F_{MOON} to retrieve the RSB F-factor, using the H-factor as an input variable. The F-factor model has one constraint: at the start of the mission, the H-factors for all angles and wavelengths are unity. Because the lunar F-factor from Equation (5) fluctuates within a year with a magnitude often exceeding 0.5%, to accurately retrieve the F-factor (often called the SD F-factor), we use multi-year lunar F-factors to feed into the model.

For the SNPP and N20 VIIRS, we fit

$$F = F(H_{\mathrm{SDSM}}) \times \frac{1 + \alpha_{\mathrm{RTA}}(1 - H_{\mathrm{SDSM}})}{1 + \alpha_{\mathrm{H}}(1 - H_{\mathrm{SDSM}}) \times \left(\phi_{\mathrm{H}} - 48^{\circ}\right)} \tag{6}$$

to the multi-year lunar F-factors in the least-squares sense, where H_{SDSM} is the SDSM RSR deconvolved, linearly interpolated at the RSB band wavelength [12,30]; ϕ_{H} is the solar

azimuth angle in the SD plane; and α_{RTA} and α_{H} are the model parameters. $F(H_{\mathrm{SDSM}})$ is the F-factor calculated in Equation (3) with H_{SDSM} instead of H_{RTA}. H_{RTA} is then approximated by

$$H_{\mathrm{RTA}} = H_{\mathrm{SDSM}} \times \frac{1 + \alpha_{\mathrm{RTA}}(1 - H_{\mathrm{SDSM}})}{1 + \alpha_{\mathrm{H}}(1 - H_{\mathrm{SDSM}}) \times (\phi_H - 48^\circ)}. \quad (7)$$

Equation (6) is actually from Equation (7) because of the RSB detector RSR's sharp central peak and the peak's dominance in the wavelength integral. Equation (7) is basically a linear functional approximation when H_{SDSM} is close to unity. In reaching Equation (7), we used the approximation that when $|x| \ll 1$, $1 - x \approx 1/(1 + x)$. Equation (7) is based on two assumptions. First, the on-orbit change in the SD surface physical property is measured by the H-factor, or equivalently by 1-H-factor, not how much time the VIIRS has been in flight. Based on the first assumption, we further assume that the relation between the H-factors at two different directions is an analytic function of the H-factor and so is the relation between the H-factors at two different SD surface positions (at the same wavelength). At the satellite launch time, the H-factors for all directions and at all wavelengths are unity, namely, $H_{\mathrm{RTA}} = H_{\mathrm{SDSM}} = H^{\mathrm{M}}_{\mathrm{SDSM}} = 1$ at $t = 0$. As the H-factor changes in time, H_{RTA} starts to differ from H_{SDSM} at shorter wavelengths within the RSBs, and the amount of difference depends on how far the H-factor is away from unity. In Equations (6) and (7), $\alpha_{\mathrm{H}} = 0.0033\left[1 - 0.076/(\lambda/\mu m)^{2.48}\right]\left[\mathrm{deg}^{-1}\right]$ for the SNPP VIIRS, also used for the N21 VIIRS. The values of α_{RTA} for the SNPP VIIRS RSBs, also used in this paper for the N21 VIIRS RSBs, are listed in Table A2 in Appendix C.

Because of the wavelength integral in Equation (3), to verify that Equation (7) yields an accurate H_{RTA}, for the SNPP VIIRS, we further fit the lunar F-factors, using

$$F = F(H_{\mathrm{RTA}}) \times [1 + \Delta\alpha_{\mathrm{RTA}}(1 - H_{\mathrm{SDSM}})], \quad (8)$$

where $F(H_{\mathrm{RTA}})$ is calculated in Equation (3) with the H_{RTA} given by Equation (7). We find that $\Delta\alpha_{\mathrm{RTA}}$ is essentially zero for nearly all the SNPP and N20 VIIRS RSBs, having very minor values for the SNPP VIIRS bands I1 and I2. Hence, for the N21 VIIRS RSBs, we use Equation (6) to retrieve the F-factor without the additional step of using Equation (8).

For the N21 VIIRS, at the time of this writing, we do not have multi-year lunar measurements. To resolve this limitation, we observe that the N21 VIIRS SDSM-measured H-factors have changed on orbit with very similar time rates to the respective SNPP VIIRS SDSM-measured H-factors. As a result, we find the N21 VIIRS RSB F-factor as

$$F(B, t; N21) = F\left[H^{\mathrm{M}}_{\mathrm{SDSM}}(B, t; N21)\right] \times \frac{F(B, t; SNPP)}{F\left[H^{\mathrm{M}}_{\mathrm{SDSM}}(B, t; SNPP)\right]}, \quad (9)$$

where B indicates a given RSB. The second term on the right side of Equation (9)

$$\frac{F(B, t; SNPP)}{F\left[H^{\mathrm{M}}_{\mathrm{SDSM}}(B, t; SNPP)\right]}$$

is essentially

$$\frac{1 + \alpha_{\mathrm{RTA}}(1 - H_{\mathrm{SDSM}})}{1 + \alpha_{\mathrm{H}}(1 - H_{\mathrm{SDSM}}) \times (\phi_{\mathrm{H}} - 48^\circ)}$$

for the SNPP VIIRS.

The SDSM-measured H-factors do not cover the wavelengths larger than 1 micrometer. Consequently, as we have done for the SNPP and N20 VIIRS [37], we use a wavelength power law:

$$H^{\mathrm{M}}_{\mathrm{SDSM}}(\lambda, t) = 1 - \frac{\beta_H(t)}{\left(\frac{\lambda}{1\ \mu m}\right)^{\eta_H(t)}}, \quad (10)$$

where the model parameters β_H and η_H are found through a least-squares fit to the SDSM-measured H-factors for detectors 5 to 8. Equation (10) is empirical, based on the fact that the strength of light scattering from materials is often in a wavelength power law form. The wavelength dependence in the equation reflects our observations that, at a longer wavelength, the H-factor is closer to unity.

3. Screen Functions Derived from Calibration Data Collected at Both the Yaw Maneuver and Regular Times

We apply the methodology developed for the SNPP VIIRS screens with a slight improvement [26,27]. The improvement is based on our earlier observation that the SDSM detector radiometric gains can depend on temperature, especially for detector 8 [16]. As a result, we normalize the SDSM detector background subtracted digital count (dc)—see Equation (12)—so that the temperature effect is removed.

The temperature's impact on the N21 VIIRS SDSM detector radiometric gain is seen from the clear positive correlation between the SDSM detector Sun-view dc and the bulkhead temperature, as shown in Figure 3 for the SDSM detector 8. To quantify the temperature's impact, we model the dc's bulkhead temperature dependence—at the solar declination angle of zero degrees in the SDSM screen coordinate system (see Appendix A)—as the following [38]:

$$dc = e^{-c_{G0}-c_{G1}(t-t_{mid})} \times [1 + c_H(\phi_{H,SDSM} - \phi_0)] \times [1 + c_T(T_{bulkhead} - T_0)] \ [DC], \quad (11)$$

where t is days since the N21 launch, $\phi_{H,SDSM}$ is the solar azimuth in the SDSM screen coordinate system (see Appendix A), and $T_{bulkhead}$ is the bulkhead temperature in Kelvin. [DC] at the end of Equation (11) is the unit. The model parameters c_{G0}, c_{G1}, c_H, and c_T are obtained through a least-squares regression. To find the parameter values, we use the SDSM Sun views from days 89 to 96 (7–14 February 2023). For this dataset, we set $t_{mid} = 89$ days, $\phi_0 = -8.67°$, and $T_0 = 259.5$ Kelvin. Only SDSM detectors 7 and 8 have impactful temperature dependence with respective c_Ts of 0.0012 and 0.0033 Kelvin^{-1}. The SDSM digital count with the temperature impact removed is then computed by

$$dc_{adj} = dc/[1 + c_T(T_{bulkhead} - T_0)]. \quad (12)$$

To refine the SDSM screen transmittance function, as we did for the SNPP and N20 VIIRS, in addition to the calibration data collected at the yaw maneuver times, we also use the calibration data from a small portion of the regular orbits. Across the regular orbits, the solar azimuth angles cover the full mission range. To reduce the adverse impact of any possible nonlinear temporal changes in the solar spectral power and the SDSM detector radiometric gains, we divide the regular on-orbit calibration data into smaller consecutive time segments. On each of these segments, the solar angle's range covers the solar angles on the corresponding yaw maneuver orbit [26,27].

On each data segment, including the data collected at the yaw maneuver time, the SDSM screen's relative effective transmittance, $\tau^R_{SDSM,eff}$, is calculated by

$$\tau^R_{SDSM,eff} = \frac{dc_{SUN,adj}(t,\ d)d^2_{VIIRS-SUN}(t)}{dc_{SUN,adj}(t_{mid},\ d)d^2_{VIIRS-SUN}(t_{mid})} \times [1 + c_{1,SDSM}\Delta t + c_{2,SDSM}\Delta t^2], \quad (13)$$

where $\Delta t = t - t_{mid}$ with t_{mid} at about the middle time in the data segment, $dc_{SUN,adj}$ is the background subtracted digital count for the SDSM detector with an index d with the temperature effect removed. $c_{1,SDSM}$ and $c_{2,SDSM}$ in Equation (13) are the corresponding Taylor-polynomial-series coefficients for the ratio of

$$\frac{dc_{sun,norm}(t_{mid}, d)}{dc_{sun,norm}(t, d)}, \quad (14)$$

where the normalized dc for the SDSM Sun view, $dc_{\text{sun,norm}}$, is defined by

$$dc_{\text{sun,norm}} = \frac{dc_{\text{sun,adj}} d^2_{\text{VIIRS}-\text{sun}}}{\tau^{\text{R}}_{\text{SDSM,eff}}\left(\vec{\phi}, d\right)}. \tag{15}$$

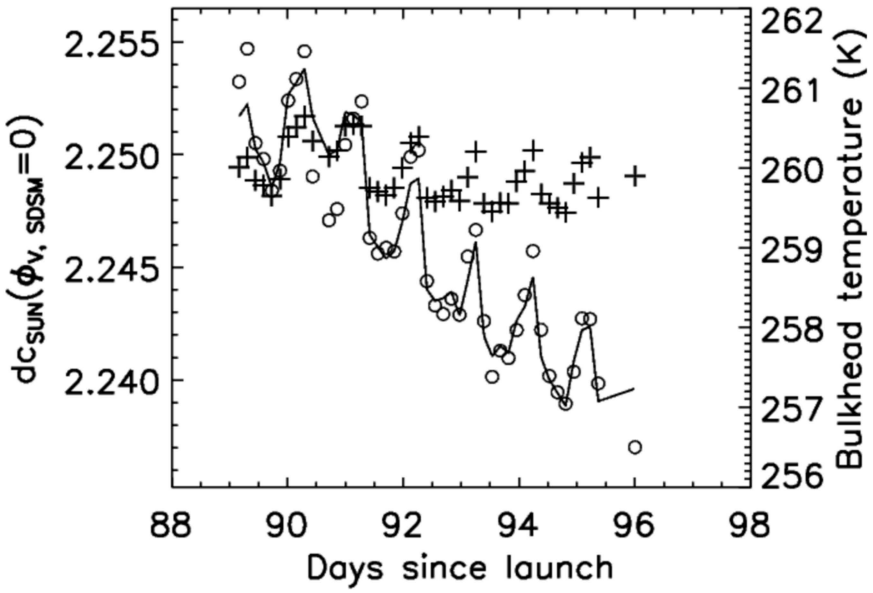

Figure 3. The N21 VIIRS SDSM detector 8 Sun-view background's subtracted digital count (circles) and the bulkhead temperature (pluses) vs. time. The solid line is the model regression (see Equation (11)).

Finding $\tau^{\text{R}}_{\text{SDSM,eff}}$ is recursive. To refine the screen functions, satellite yaw maneuvers were performed within one day on satellite orbits 1649–1663. We first refine the screen function with the calibration data from the yaw maneuver orbits alone. We use the prelaunch SDSM screen transmittance to feed into Equation (15) to find $c_{1,\text{SDSM}}$ and $c_{2,\text{SDSM}}$. Then, we use the calibration data collected on the yaw maneuver orbits to refine $\tau^{\text{R}}_{\text{SDSM,eff}}$. Using the refined $\tau^{\text{R}}_{\text{SDSM,eff}}$ in Equation (15), we update $c_{1,\text{SDSM}}$ and $c_{2,\text{SDSM}}$, which are then used in Equation (13) to update $\tau^{\text{R}}_{\text{SDSM,eff}}$. At this step, we finish refining $\tau^{\text{R}}_{\text{SDSM,eff}}$ with the data from the yaw maneuver orbits. We use $\tau^{\text{R}}_{\text{SDSM,eff}}(\text{yaw})$ to denote this $\tau^{\text{R}}_{\text{SDSM,eff}}$.

By mission day 381 (26 November 2023), we encountered sufficient high-quality regular calibration data whose solar angles cover the full mission range. The data are "high-quality" in that, within the least amount of time, the solar angles in the data cover what is expected for the angles over the mission. The "least amount of time" reduces the time duration for each regular data segment to minimize the adverse impact of any possible nonlinear temporal changes in the solar power and the SDSM detector gains. The regular calibration data that we select to refine the SDSM screen function are from days 219 to 381. We divide the data into 14 consecutive segments. We use Equation (13) to update $\tau^{\text{R}}_{\text{SDSM,eff}}$ over the solar angles on each of the segments, denoted by $\tau^{\text{R}}_{\text{SDSM,eff}}(\text{regular})$. Then, we scale $\tau^{\text{R}}_{\text{SDSM,eff}}(\text{regular})$ to match $\tau^{\text{R}}_{\text{SDSM,eff}}(\text{yaw})$ over the solar angles on the corresponding yaw maneuver orbit when the SDSM observes the Sun through the SDSM screen. On these regular data segments, the $c_{1,\text{SDSM}}$ obtained with $\tau^{\text{R}}_{\text{SDSM,eff}}(\text{yaw})$ may not be accurate enough. We refine $c_{1,\text{SDSM}}$ based on the fact that, on the orbit shared by neighboring regular data segments, $\tau^{\text{R}}_{\text{SDSM,eff}}(\text{regular})$ from these two segments should be the same [26]. With the updated $c_{1,\text{SDSM}}$, we find $\tau^{\text{R}}_{\text{SDSM,eff}}(\text{regular})$ again and scale it to match $\tau^{\text{R}}_{\text{SDSM,eff}}(\text{yaw})$ over the solar angles on the corresponding yaw maneuver orbit.

To reach the final SDSM screen's relative effective transmittance, $\tau^{\mathrm{R}}_{\mathrm{SDSM,eff}}$, we combine $\tau^{\mathrm{R}}_{\mathrm{SDSM,eff}}(\mathrm{yaw})$ with $\tau^{\mathrm{R}}_{\mathrm{SDSM,eff}}(\mathrm{regular})$ and interpolate the transmittance at evenly stepped solar angles in both the solar declination and azimuth angles in the SDSM screen coordinate system. We use $\tau^{\mathrm{R}}_{\mathrm{SDSM,eff}}(\mathrm{yaw}+\mathrm{regular})$ to denote this final SDSM screen transmittance function.

We refine the product of the SD screen's relative effective transmittance and the BRDF for the SDSM SD view, denoted by $\tau^{\mathrm{R}}_{\mathrm{SD,eff}}\mathrm{BRDF}_{\mathrm{SDSM}}$, using only the data collected on the yaw maneuver orbits. We expect the refined $\tau^{\mathrm{R}}_{\mathrm{SD,eff}}\mathrm{BRDF}_{\mathrm{SDSM}}$ to be of high accuracy because of the large number of through holes on the SD screen that allows sunlight to be scattered by the SD and received by an SDSM detector. We calculate $\tau^{\mathrm{R}}_{\mathrm{SD,eff}}\mathrm{BRDF}_{\mathrm{SDSM}}$ through [27]

$$\begin{aligned}&\tau^{\mathrm{R}}_{\mathrm{SD,eff}}\left(\vec{\phi}(t),d\right)\mathrm{BRDF}_{\mathrm{SDSM}}\left(\lambda_d,t=0,\vec{\phi}(t)\right)\\&=\frac{dc_{\mathrm{SD,adj}}(t,d)d^2_{\mathrm{VIIRS-sun}}(t)\sin\phi_{\mathrm{V,SD}}(t_{\mathrm{mid}})}{dc_{\mathrm{SD,adj}}(t_{\mathrm{mid}},d)d^2_{\mathrm{VIIRS-sun}}(t_{\mathrm{mid}})\sin\phi_{\mathrm{V,SD}}(t)}\times\left[1+c_{1,\mathrm{SDSM}}(t-t_{\mathrm{mid}})+c_{2,\mathrm{SDSM}}(t-t_{\mathrm{mid}})^2\right]\times\\&\frac{1}{1+\frac{\partial H_{\mathrm{SDSM}}}{H_{\mathrm{SDSM}}\partial t}\Big|_{t\mathrm{mid}}\Delta t+\frac{\partial^2 H_{\mathrm{SDSM}}}{2H_{\mathrm{SDSM}}\partial t^2}\Big|_{t\mathrm{mid}}\Delta t^2+\frac{\partial H_{\mathrm{SDSM}}}{H_{\mathrm{SDSM}}\partial\phi_{\mathrm{V,SD}}}\Big|_{t\mathrm{mid}}(\phi_{\mathrm{V,SD}}(t)-\phi_{\mathrm{V,SD}}(\mathrm{t_{mid}}))}\end{aligned}\tag{16}$$

where $dc_{\mathrm{SD,adj}}$ is the SDSM detector d digital count for the SD view with background subtracted and the temperature effect removed. In Equation (16), the time derivatives of the true H-factor for the SDSM SD view are approximated by the time derivatives of the SDSM-measured H-factor, $H^{\mathrm{M}}_{\mathrm{SDSM}}$, derived by using $\tau^{\mathrm{R}}_{\mathrm{SDSM,eff}}(\mathrm{yaw}+\mathrm{regular})$. We approximate the derivative of the H-factor with respect to $\phi_{\mathrm{V,SD}}$, using the value obtained for the SNPP VIIRS SD, because of the very similar on-orbit temporal change rates between the SNPP and N21 VIIRS SD H-factors at the same wavelength and the time since the respective mission starts, given by [27,30]:

$$\left.\frac{\partial H_{\mathrm{SDSM}}}{\partial\phi_{\mathrm{V,SD}}}\right|_{t\mathrm{mid}}=0.0005145\times\left[1-H^{\mathrm{M}}_{\mathrm{SDSM}}(d;t_{\mathrm{mid}})\right]-0.00212\times\left[1-H^{\mathrm{M}}_{\mathrm{SDSM}}(d;t_{\mathrm{mid}})\right]^2.\tag{17}$$

The functional form of Equation (17) comes from the same assumptions as those for Equation (7). The angular dependence strength of the H-factor, in this case H_{SDSM}, depends on the change in the physical property of the SD surface. The change in the SD surface physical property is measured by the H-factor. And the angular dependence is an analytic function of the H-factor.

Similarly, we refine the relative product of the SD screen transmittance and the BRDF for the RTA SD view, denoted by $\tau^{\mathrm{R}}_{\mathrm{SD}}\mathrm{BRDF}_{\mathrm{RTA}}$, using the data collected only on the yaw maneuver orbits. We calculate $\tau^{\mathrm{R}}_{\mathrm{SD}}\mathrm{BRDF}_{\mathrm{RTA}}$ through [27,28,30]

$$\begin{aligned}&\boldsymbol{\tau^{\mathrm{R}}_{\mathrm{SD}}\mathrm{BRDF}_{\mathrm{RTA}}}\left(\boldsymbol{\lambda_{\mathrm{B}},t=0,\vec{\phi}(t)}\right)\\&=\frac{F(t,d)P(dn_{\mathrm{SD}}(t))}{F(t_{\mathrm{mid}},d)P(dn_{\mathrm{SD}}(t_{\mathrm{mid}}))}\times\frac{d^2_{\mathrm{VIIRS-sun}}(t)\sin\phi_{\mathrm{V,SD}}(t_{\mathrm{mid}})}{d^2_{\mathrm{VIIRS-sun}}(t_{\mathrm{mid}})\sin\phi_{\mathrm{V,SD}}(t)}\times\frac{\int_0^\infty d\lambda\times\mathrm{RSR}(\lambda,t_{\mathrm{mid}},d)\Phi_{\mathrm{sun}}(\lambda,t_{\mathrm{mid}})H_{\mathrm{RTA}}\left(\lambda,t_{\mathrm{mid}},\vec{\phi}(t_{\mathrm{mid}})\right)}{\int_0^\infty d\lambda\times\mathrm{RSR}(\lambda,t,d)\Phi_{\mathrm{sun}}(\lambda,t)H_{\mathrm{RTA}}\left(\lambda,t,\vec{\phi}(t)\right)},\end{aligned}\tag{18}$$

where λ_{B} is the band center wavelength and d is the detector index in the band. The F-factor ratio on the right side of Equation (18) is nearly unity because the time span over the yaw maneuver orbits is short: less than one day. We use the F-factor calculated with the prelaunch screen function to find the F-factor ratio. For the shortwave-infrared (SWIR) bands, the H-factors are close to unity. As a result, for these bands, the ratio of the wavelength integrals on the right side of Equation (18) approximates to one. For the visible near-infrared (VisNIR) bands, the ratio of the integrals essentially has three contributions which relate to the H-factor's time and solar angular dependence (the RSR is a stable

function of time because the F-factors calculated with the prelaunch screen functions do not strongly depend on time) approximated by

$$\frac{\int_0^\infty d\lambda \times \mathrm{RSR}(\lambda, t_{\mathrm{mid}}, d)\Phi_{\mathrm{sun}}(\lambda, t_{\mathrm{mid}})H_{\mathrm{RTA}}\left(\lambda, t_{\mathrm{mid}}, \vec{\phi}(t_{\mathrm{mid}})\right)}{\int_0^\infty d\lambda \times \mathrm{RSR}(\lambda, t, d)\Phi_{\mathrm{sun}}(\lambda, t)H_{\mathrm{RTA}}\left(\lambda, t, \vec{\phi}(t)\right)} = \frac{1}{1 + \frac{\partial H_{\mathrm{RTA}}}{H_{\mathrm{RTA}}\partial t}\Big|_{t\mathrm{mid}}\Delta t + \frac{\partial^2 H_{\mathrm{RTA}}}{2H_{\mathrm{RTA}}\partial t^2}\Big|_{t\mathrm{mid}}\Delta t^2 + \frac{\partial H_{\mathrm{RTA}}}{H_{\mathrm{RTA}}\partial \vec{\phi}}\Big|_{t\mathrm{mid}} \cdot \left(\vec{\phi}(t) - \vec{\phi}(t_{\mathrm{mid}})\right)}. \tag{19}$$

The time derivative of H_{RTA} at the yaw maneuver time contributes little, by less than 0.04% with a larger derivative magnitude at a shorter wavelength. Hence, we use the time derivatives for bands M1–M4 only.

Because the N21 VIIRS $H^{\mathrm{M}}_{\mathrm{SDSM}}$ changes in time at very similar rate to that for the SNPP VIIRS, we use the solar angular dependence obtained for the SNPP VIIRS SD H-factor here [30]:

$$\frac{\partial H_{\mathrm{RTA}}}{H_{\mathrm{RTA}}\left(\lambda_{\mathrm{B}}, t_{\mathrm{mid}}, \vec{\phi}(t_{\mathrm{mid}})\right)\partial\phi_{\mathrm{V,SD}}} = \frac{0.0041 \times \left(1 - H^{\mathrm{M}}_{\mathrm{SDSM}}\right)}{H^{\mathrm{M}}_{\mathrm{SDSM}}} \text{ per degree} \tag{20}$$

and

$$\frac{\partial H_{\mathrm{RTA}}}{H_{\mathrm{RTA}}\left(\lambda_{\mathrm{B}}, t_{\mathrm{mid}}, \vec{\phi}(t_{\mathrm{mid}})\right)\partial\phi_{\mathrm{H,SD}}} = \frac{0.0033 \times \left(1 - 0.076/\lambda_B^{2.48}\right) \times \left(1 - H^{\mathrm{M}}_{\mathrm{SDSM}}\left(\lambda_{\mathrm{B}}, t_{\mathrm{mid}}, \vec{\phi}(t_{\mathrm{mid}})\right)\right)}{H^{\mathrm{M}}_{\mathrm{SDSM}}\left(\lambda_{\mathrm{B}}, t_{\mathrm{mid}}, \vec{\phi}(t_{\mathrm{mid}})\right)} \text{ per degree} \tag{21}$$

In Equation (21), the band wavelength is in micrometers and $H^{\mathrm{M}}_{\mathrm{SDSM}}$ is linearly interpolated at λ_{B}, t_{mid}, and $\phi_{\mathrm{V,SD}}(t_{\mathrm{mid}})$. The H-factor solar angular dependence strength is wavelength-dependent: the shorter the wavelength, the larger the dependence. At the yaw maneuver time, for band M1 (shortest band center wavelength among the VIIRS RSBs), Equations (20) and (21) give the H_{RTA} solar declination and azimuth angular dependences of 0.0004 per degree and 0.0001 per degree, respectively.

Finally, to find $\tau_{\mathrm{SD}}\mathrm{BRDF}_{\mathrm{RTA}}$, we scale the retrieved $\tau^{\mathrm{R}}_{\mathrm{SD}}\mathrm{BRDF}_{\mathrm{RTA}}$ to match the prelaunch $\tau_{\mathrm{SD}}\mathrm{BRDF}_{\mathrm{RTA}}$ over the calibration sweet spot in a least-squares sense.

For simplicity, we use $\tau^{\mathrm{R}}_{\mathrm{SD,eff}}\mathrm{BRDF}_{\mathrm{SDSM}}(\mathrm{yaw})$ and $\tau_{\mathrm{SD}}\mathrm{BRDF}_{\mathrm{RTA}}(\mathrm{yaw})$ to denote $\tau^{\mathrm{R}}_{\mathrm{SD,eff}}\left(\vec{\phi}(t),\, d\right)\mathrm{BRDF}_{\mathrm{SDSM}}\left(\lambda_d, t = 0, \vec{\phi}(t)\right)$ and $\tau^{\mathrm{R}}_{\mathrm{SD}}\mathrm{BRDF}_{\mathrm{RTA}}\left(\lambda_{\mathrm{B}},\, t = \mathbf{0}, \vec{\phi}(t)\right)$, respectively, derived from the calibration data collected on the yaw maneuver orbits.

4. Results

4.1. Screen Functions

By using the calibration data collected from both the yaw maneuver and the regular times, the SDSM screen's relative effective transmittance has been improved significantly. As an example, in Figure 4 for SDSM detector 8 at $\phi_{\mathrm{V,SDSM}} = 0$, we compare the prelaunch SDSM screen function, $\tau^{\mathrm{R}}_{\mathrm{SDSM,eff}}(\mathrm{prelaunch})$, the SDSM screen function derived from the data collected at the yaw maneuver time, $\tau^{\mathrm{R}}_{\mathrm{SDSM,eff}}(\mathrm{yaw})$, and the screen function derived from the data collected at both the yaw maneuver and the regular times, $\tau^{\mathrm{R}}_{\mathrm{SDSM,eff}}(\mathrm{yaw} + \mathrm{regular})$. The figure shows that (1) $\tau^{\mathrm{R}}_{\mathrm{SDSM,eff}}(\mathrm{yaw} + \mathrm{regular})$ improves upon $\tau^{\mathrm{R}}_{\mathrm{SDSM,eff}}(\mathrm{yaw})$ by more than 1% around the solar azimuth angle (SDSM screen coordinate system) of -11.1° and (2) $\tau^{\mathrm{R}}_{\mathrm{SDSM,eff}}(\mathrm{yaw})$ improves upon $\tau^{\mathrm{R}}_{\mathrm{SDSM,eff}}(\mathrm{prelaunch})$ by more than 1% around the solar azimuth angle of -2.8°.

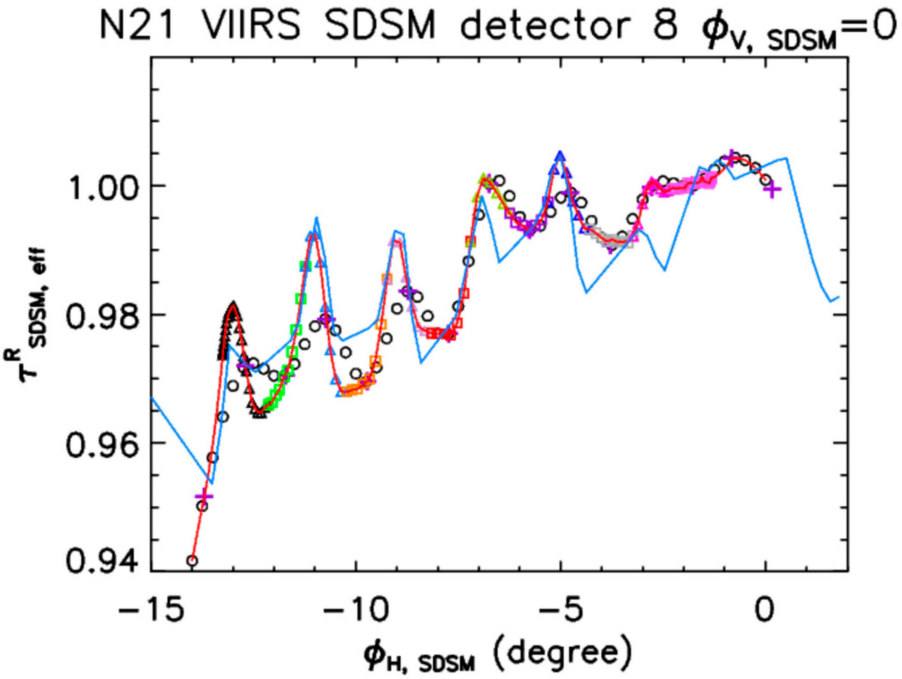

Figure 4. The N21 VIIRS SDSM screen's relative effective transmittance for detector 8, $\tau^{R}_{SDSM,eff}$ vs. the solar azimuth angle in the SDSM screen's coordinate system at the solar declination angle $\phi_{V,SDSM} = 0$: prelaunch values (blue solid line), values derived from the Sun-view data on the yaw maneuver orbits (black circles), and values derived from the Sun-view data on both the yaw maneuver and regular orbits (other symbols and red solid line).

Our retrieved product of the SD screen's relative effective transmittance and the SD BRDF at the start of the mission for the SDSM SD view, $\tau^{R}_{SD,eff}BRDF_{SDSM}(yaw)$, does not differ much from the prelaunch values, as illustrated in Figure 5 for SDSM detector 1. Compared with the case for the SDSM screen, this much smaller difference is due to the much larger number of through holes—hundreds—on the SD screen through which sunlight passes before being scattered onto an SDSM detector. When the solar vector moves with respect to the VIIRS, the number of the SD screen's through holes sensed by an SDSM detector can change slightly, maybe by one or two, which is a small percentage of the hundreds of through holes. On the contrary, the nominal number of the SDSM screen's through holes sensed by an SDSM detector is only 16. When one through hole is in or out of an SDSM detector's Sun view, the change is 1 out of 16, a large 6.26% change.

The product of the SD screen transmittance and the BRDF for the RTA SD view at the start of the mission derived from the calibration data collected at the yaw maneuvers, $\tau_{SD}BRDF_{RTA}(yaw)$, also differs only slightly from the prelaunch values. Along the solar declination angle from 14° to 18°, the difference between the prelaunch and the yaw maneuver data derived $\tau_{SD}BRDF_{RTA}$ is less than 0.26%, as shown in Figure 6 for band M1.

The prelaunch $\tau_{SD}BRDF_{RTA}$ for band M11 is extrapolated from laboratory measurements which do not go beyond the center wavelength of band M10 of about 1.6 μm [33]. A significant difference was seen in the retrieved lunar irradiances between the N20 and the N21 VIIRS Collection 1.0 band M11 (see Table 3), with the retrieved lunar irradiance from the N21 VIIRS smaller by 6.1% than that from the N20 VIIRS. The prelaunch $\tau_{SD}BRDF_{RTA}$ was measured at only a few wavelengths, with much more noise for the N21 than the N20 VIIRS. Hence, we believe that the extrapolation for the N21 VIIRS $\tau_{SD}BRDF_{RTA}$ to the band M11 wavelength of 2.25 μm is rather inaccurate, thus we adjust the N21 VIIRS $\tau_{SD}BRDF_{RTA}$ at the wavelength upwards by 6.1%. The NOAA VIIRS calibration team also performed an upward adjustment for the N21 VIIRS prelaunch $\tau_{SD}BRDF_{RTA}$ for band M11 (as well as the other SWIR bands) but with a different magnitude [39].

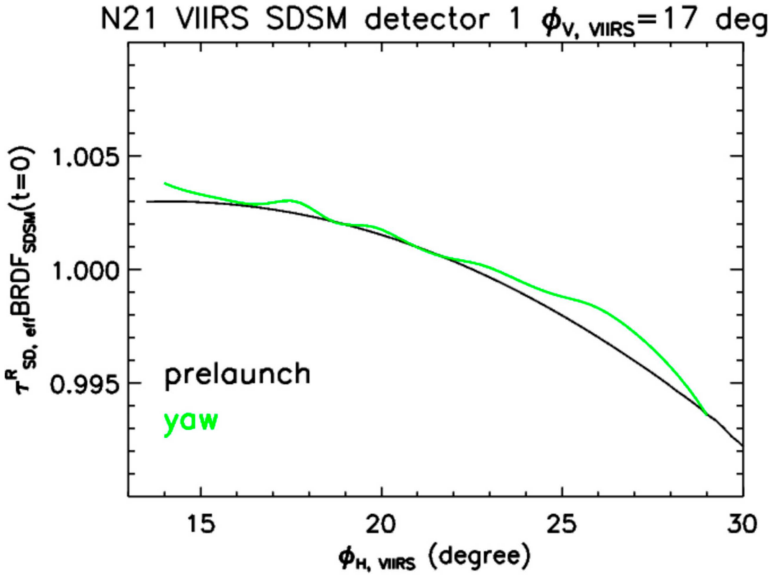

Figure 5. The N21 VIIRS SD screen's relative effective transmittance times the SD BRDF for the SDSM SD view at the start of the mission for the SDSM detector 1, $\tau^{R}_{SD,eff}BRDF_{SDSM}$, vs. the solar azimuth angle in the VIIRS coordinate system (see Appendix A) at the solar declination angle $\phi_{V,VIIRS}$ = 17°: prelaunch values (black solid line) and values derived from the calibration data collected on the yaw maneuver orbits (green solid line).

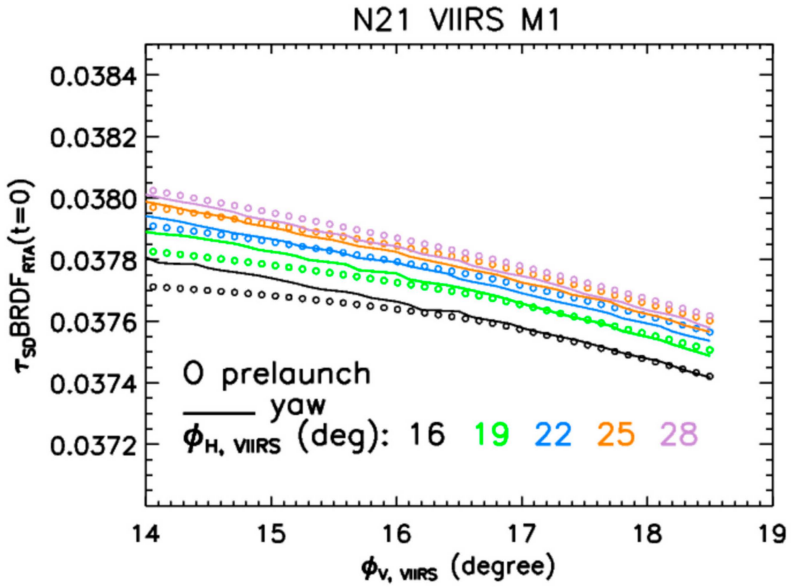

Figure 6. The N21 VIIRS SD screen transmittance times the SD BRDF for the telescope SD view at the start of the mission for the VIIRS band M1, $\tau_{SD}BRDF_{RTA}$, vs. the solar declination angle in the VIIRS coordinate system at five solar azimuth angles, 16°, 19°, 22°, 25°, and 28°: prelaunch values (circles) and values derived from the calibration data collected on the yaw maneuver orbits (solid lines).

4.2. SDSM and SD Radiometric Calibration Performance

The N21 VIIRS SDSM detector radiometric gains decrease with time, as do the SNPP and N20 VIIRS SDSM detectors, as shown in Figure 7. The gain of SDSM detector 8 decreases the most across the three VIIRS instruments, whereas the gains of detectors 3–5 decrease the least, a result of the combination of the SDSM Spherical Integrating Source's BRDF degradation with time, larger at a short wavelength, and the SDSM detector lattice damage from solar particles, larger at a longer wavelength [40,41]. The SDSM fold mirror reflectivity's change in time also contributes to the overall SDSM detector gain change.

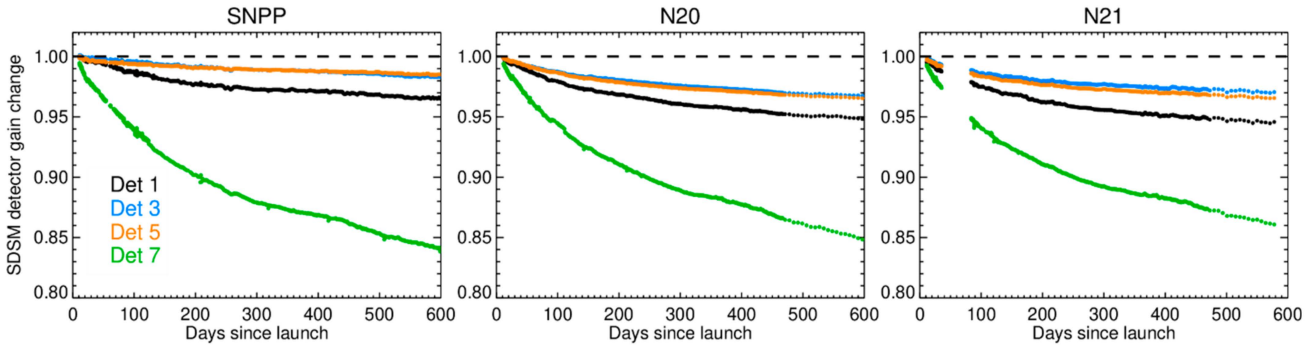

Figure 7. The SDSM detector's radiometric gains vs. the respective days since the satellite launch, normalized to the satellite launch time, for the SNPP (**left**), N20 (**center**), and N21 (**right**) VIIRS instruments.

The accuracy improvement in the SDSM Sun-view screen's relative effective transmittance is clearly shown in Figure 8. The prelaunch screen transmittance is the least accurate, resulting in the largest unexpected undulations in the measured H-factor versus time curves, as shown in the left chart in Figure 8. The screen transmittance function is improved by using the calibration data collected at the yaw maneuver time, reflecting reduced undulations in the measured H-factor versus time curves, as shown in the middle chart in the figure. The screen transmittance function derived from the calibration data collected at both the yaw maneuver and the regular times is the most accurate, yielding much smoother H-factor versus time curves, as shown in the right chart in the figure.

The SDSM-measured SD BRDF on-orbit change factors (without SDSM detector RSR deconvolution), the H-factors, generally trend downwards in time, larger at a shorter wavelength, just as they do for the SNPP and N20 VIIRS SDs. The N21 VIIRS SDSM-measured H-factors trend downwards at very similar rates to those for the SNPP VIIRS, much faster than those for the N20 VIIRS, as shown in Figure 9. The N20 VIIRS SD surface may have less contaminants, and thus, its BRDF changes less on orbit when bombarded by the Sun.

An accurate SDSM Sun-view screen transmittance function not only improves the smoothness of the H-factor versus time curves but also the absolute accuracy of the measured H-factors. The reason for this is that we do not have calibration data in the very early mission, from the satellite launch to the first SDSM measurement, and we need to extrapolate the measured H-factors to the start of the mission ($t = 0$) and set the extrapolated H-factor at the start of the mission to unity to find the scale factor associated with the raw measured H-factors. The slope of the extrapolation, and hence the scale factor, strongly depend on the accuracy of the SDSM Sun-view screen function.

The SDSM-measured H-factors at the SWIR wavelengths are computed through the wavelength power law, defined in Equation (10), with the power law exponent η_H slowly moving upwards in time and leveling off around 4 for all three VIIRS SDs, as shown in Figure 10. At the SWIR band wavelengths, as for the H-factors over the VisNIR band wavelengths, the power law yields that, at a shorter wavelength, the H-factor decreases with time faster, namely, the temporal decrease in the H-factor at the band M8 wavelength (1.24 μm) is faster than the H-factor at the band M9 wavelength (1.38 μm). Nevertheless, the H-factors at the SWIR band wavelengths have all been very close to unity thus far in the mission. At the band M8 wavelength on mission day 500, the H-factor is less than 0.24% below one.

The strength of the H-factor angular dependence depends on wavelength, with a stronger dependence at a shorter wavelength. At a SWIR band wavelength, the difference between the H-factors for the SDSM and the RTA SD views is essentially zero (less than 0.01%), and hence, α_{RTA} is essentially zero at the SWIR wavelengths. At a VisNIR wavelength and $t > 0$, the H-factor for the RTA SD view, H_{RTA}, is larger than the H-factor at the SDSM SD view, H_{SDSM}, because the RTA SD view is in a forward-scattering geometry, whereas the SDSM SD view is in a backward-scattering geometry.

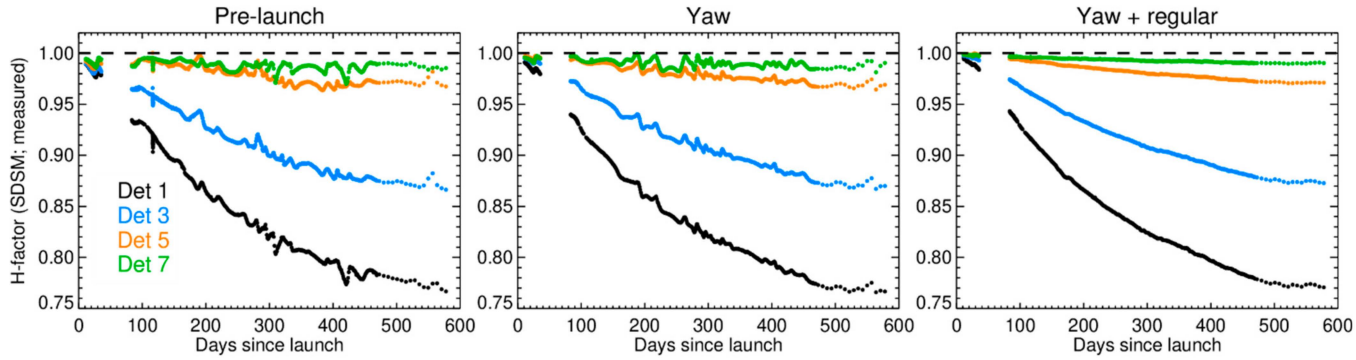

Figure 8. The measured N21 VIIRS SDSM SD BRDF on-orbit change factors, the H-factors, normalized to the satellite launch time, with the prelaunch screen transmittance functions (**left**), the screen functions derived from the yaw maneuver calibration data (**center**), and the screen functions derived from the yaw maneuver and the regular on-orbit calibration data (**right**).

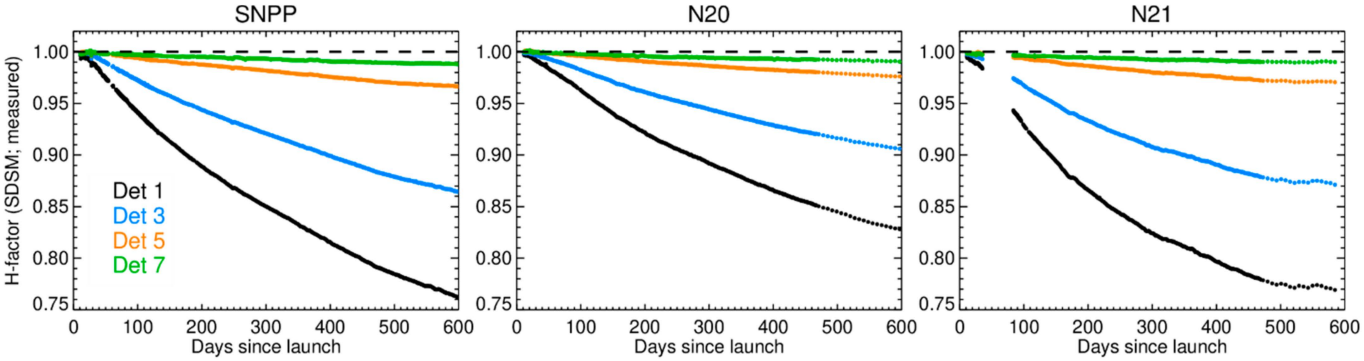

Figure 9. The measured SDSM SD BRDF on-orbit change factors, the H-factors vs. the respective days since the satellite launch, normalized to the respective launch times, for the SNPP (**left**), N20 (**center**), and N21 (**right**) VIIRS instruments.

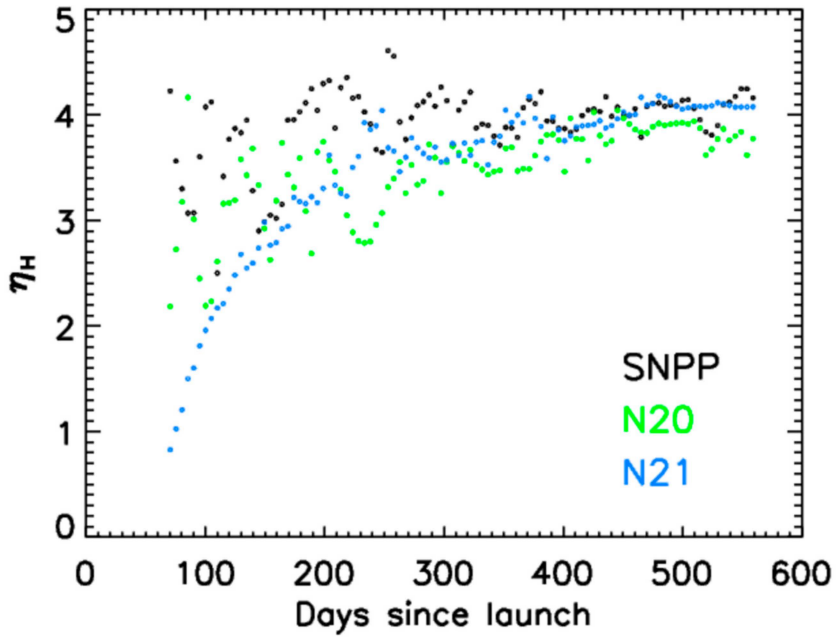

Figure 10. The wavelength power law exponents, for the SD BRDF on-orbit change factors at the SWIR wavelengths vs. the respective days since the satellite launch for the SNPP (black), N20 (green), and N21 (blue) VIIRS instruments.

4.3. RSB Radiometric Gain Performance

The N21 VIIRS RSB radiometric gain performance is measured by its F-factors, the correction factor to the *dn* polynomial that retrieves the scene spectral radiance with the prelaunch polynomial coefficients. The F-factors are calculated with the TSIS-1 hybrid solar reference spectrum (HSRS) [42,43] which can impact the F-factor by up to 2.9% and 4.2%, respectively, comparing with the MODTRAN 4.3 [44] and the Thuillier's [45] solar spectral powers currently used for the SNPP and the N20 VIIRS RSB calibrations. The TSIS-1 HSRS has an accuracy of 0.5% from 0.4 to 0.46 μm and 0.3% from 0.46 to 2.365 μm. But the solar spectral power difference does not meaningfully impact the retrieved Earth-view reflectance because the solar power appears in both the scene's spectral radiance calculation and in the denominator for the incoming solar irradiance. Like N20, the previous N21 collections, including Collection 2.0, used the Thuillier's solar spectral power. But we have switched to TSIS-1 for Collection 2.1 for improved accuracy in the radiance products. Future NASA N20 and SNPP VIIRS L1B collections will likely also switch to TSIS-1 for consistency. The digital count polynomial coefficients for a scene's spectral radiance for band M4 at the low-gain stage has also been improved with the coefficient values provided by the NOAA VIIRS calibration team.

The N21 VIIRS VisNIR band F-factors averaged across the band detectors range from 0.93 to 0.98, as shown in Figure 11, indicating a substantially improved prelaunch measurement compared with the SNPP and N20 VIIRS [12,41]. The VisNIR band F-factors have been quite stable in time, as expected based on the experience gained from previous works on the SNPP and N20 VIIRS [12,41,46,47]. The large radiometric degradation of some of the SNPP VIIRS RSBs is due to the inadvertent deposition of tungsten oxides on the four RTA mirrors coupled with solar exposure [47]. Without any tungsten oxides on the N20 and N21 RTA mirrors, the F-factors are rather flat across time.

The N21 VIIRS SWIR band F-factors have upward temporal trends during most of the time prior to the start of the second mid-mission outgassing (mission day 474), as shown in the left chart in Figure 12, perhaps because of the ice or other contaminants accumulated on the dewar walls of the short-/midwave-infrared (S/MWIR) focal plane. The upward trend means a decreasing detector radiometric gain. The increase in the F-factors for the SWIR bands was evident soon after the S/MWIR detector focal plane was cooled to 82 K. To remove the ice, mid-mission outgassing was performed from orbits 1485 to 1519 on mission days 106 to 108. Immediately after the outgassing, the F-factors for these SWIR bands returned to their respective at-launch values. However, less than 10 days after the outgassing, the F-factors started to trend upwards again, especially for bands M8 and M9, as shown in the left chart in Figure 12. On orbit 6715 (mission day 474), band M8 F-factor—averaged across the 16 detectors—increased by approximately 25% from its value at orbit 1520. To restore the radiometric gains of the SWIR bands, a second mid-mission outgassing was performed during orbits 6715 to 6743 (days 474 to 476). Since the second outgassing, the SWIR band F-factors have remained stable, as shown in Figure 12.

The ice accumulation is highly non-uniform across the SWIR band detectors. For example, just before the second mid-mission outgassing at orbit 6715 (day 474), the spread of the band M9 F-factors across the 16 detectors is multiple times wider than the spread at the end of the first mid-mission outgassing at orbit 1520 (day 108), as shown in the right chart in Figure 12. The ice accumulation of the N21 VIIRS occurred for the S/MWIR focal plane only. Focal plane ice accumulation was also seen in the early days of the N20 VIIRS operation. The N20 VIIRS ice accumulation, however, was on the longwave-infrared focal plane and was completely removed after just one mid-mission outgassing [48].

Although we did not use F_{MOON} to directly find H_{RTA} from the measured SDSM H-factor because of the limited number of lunar observations so far in the mission, we did compare the F-factors from the SD and the lunar observations. As shown in Figure 13, the respective scaled 1/F-factors from the SD and lunar observations agree within 1%. Note that to find the F-factors from the SD observations, we have relied on the ratio of the SNPP VIIRS F-factor calculated with $\mathrm{H_{RTA}}$ to the F-factor calculated with the SDSM-measured

H-factor. We will recalculate the N21 VIIRS SD F-factors again once we have multi-year lunar F-factors.

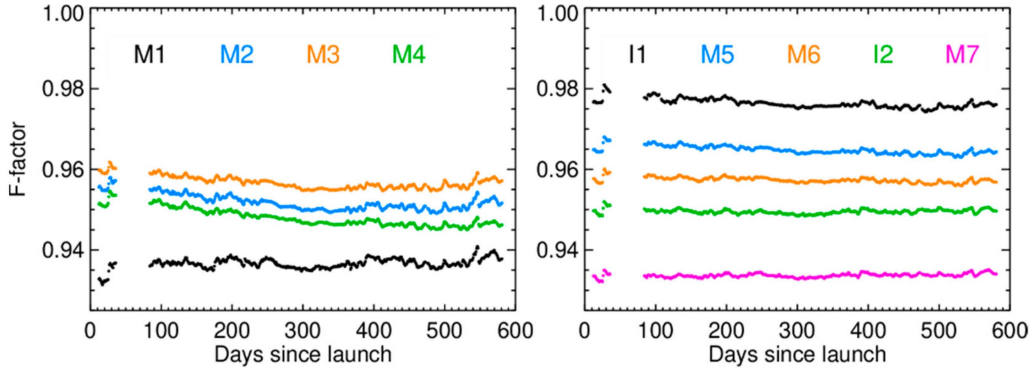

Figure 11. The N21 VIIRS VisNIR band F-factors, the correction factor to the scene spectral radiance retrieved by the quadratic detector digital number polynomial, averaged across the detectors in each band vs. days since the satellite launch. The large data gap roughly between days 37 to 85 is due to a Ka-band data transmitter malfunction.

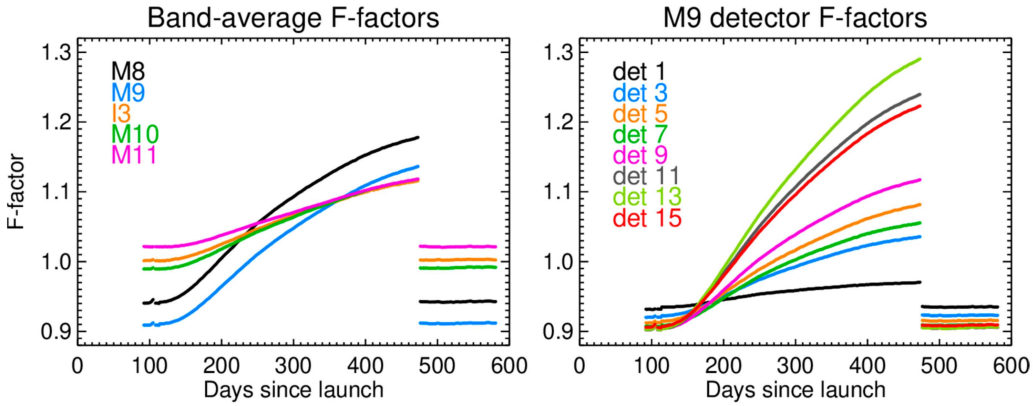

Figure 12. (**left**) The N21 VIIRS SWIR band F-factors, the correction factor to the scene spectral radiance retrieved by the quadratic detector digital number polynomial, averaged across the detectors in each band vs. days since the satellite launch. (**right**) The N21 VIIRS band M9 F-factors for detectors 1, 3, 5, 7, 9, 11, 13, and 15 vs. days since the satellite launch.

To show the F-factor trend difference among Collections 1.0, 2.0, and 2.1, as an example in Figure 14 we plot the F-factor divided by its value at orbit 180 for bands M1, M3, and M5. The F-factor in Collection 1.0 trends downwards for these bands because the SDSM-measured H-factor is used for the H-factor for the telescope SD view. The F-factor for Collection 2.0 trends slightly downwards for bands M1 and M3, whereas the F-factor for Collection 2.1 trends nearly flat in time.

In Collection 2.1, we use the TSIS-1 solar spectral power, whereas in the prior collections, we use the Thuillier solar spectral power. The largest impact of using the TSIS-1 solar spectral power on the value of the retrieved F-factor was observed for band M11, making a difference of slightly over 4%, as shown in Figure 15. Overall, the largest impacts were observed for the SWIR bands, except band M8.

The accuracy of the retrieved F-factors can also be evaluated against the retrieved top-of-the-atmosphere (TOA) spectral reflectance from pseudo-invariant sites, such as Libya 4, and deep convective clouds (DCCs). The true reflectance from these sites is expected to be very stable over time [49–51]. An incorrect F-factor temporal trend results in a reflectance temporal drift. Although at the time of this writing we do not have the official C2.1 reflectance, we find the C2.1 reflectance multiplying the C2.0 reflectance by the F-factor ratio of C2.1 to C2.0.

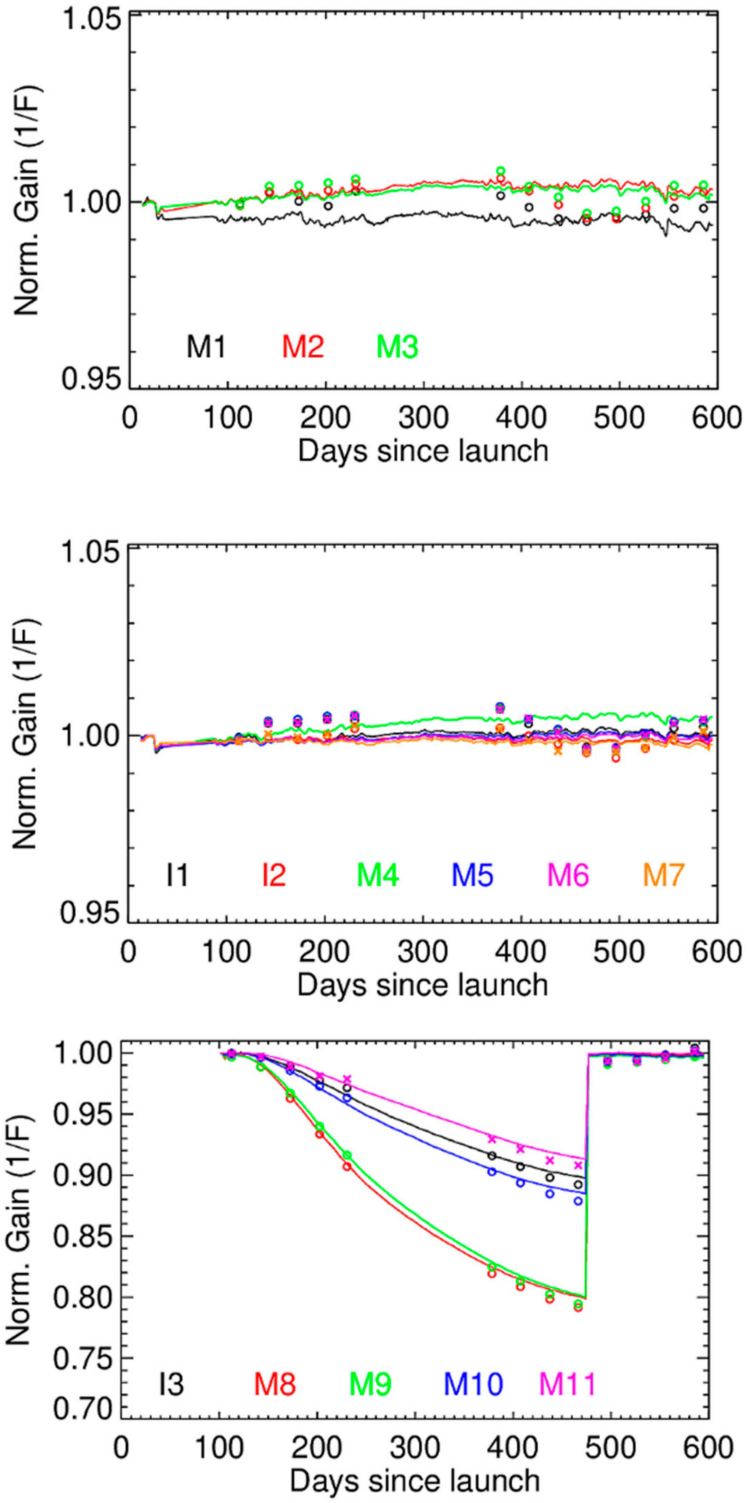

Figure 13. The N21 VIIRS RSB gains (1/F-factors) determined from the SD (solid lines) and lunar observations (circles) vs. days since the satellite launch, normalized to the respective values at orbit 180 for the SD F-factors and on 2 March 2023 (day 112) for the lunar F-factors.

The DCC reflectance is from the eastern Indian and western Pacific Oceans (20°S–20°N and 95°E–175°E) binned over a month-long dataset. The DCC reflectance of the N21 VIIRS M-bands has an upward trend of 1 to 2% from days 77 to 377, as shown in Figure 16. Note that band M6 detectors are saturated for the DCC scenes. Figure 16 reveals that the retrieved DCC L1B reflectance is influenced by solar angles. Hence, to reliably know the

DCC reflectance temporal trend, as is the case for the lunar F-factors, we need a multi-year DCC dataset.

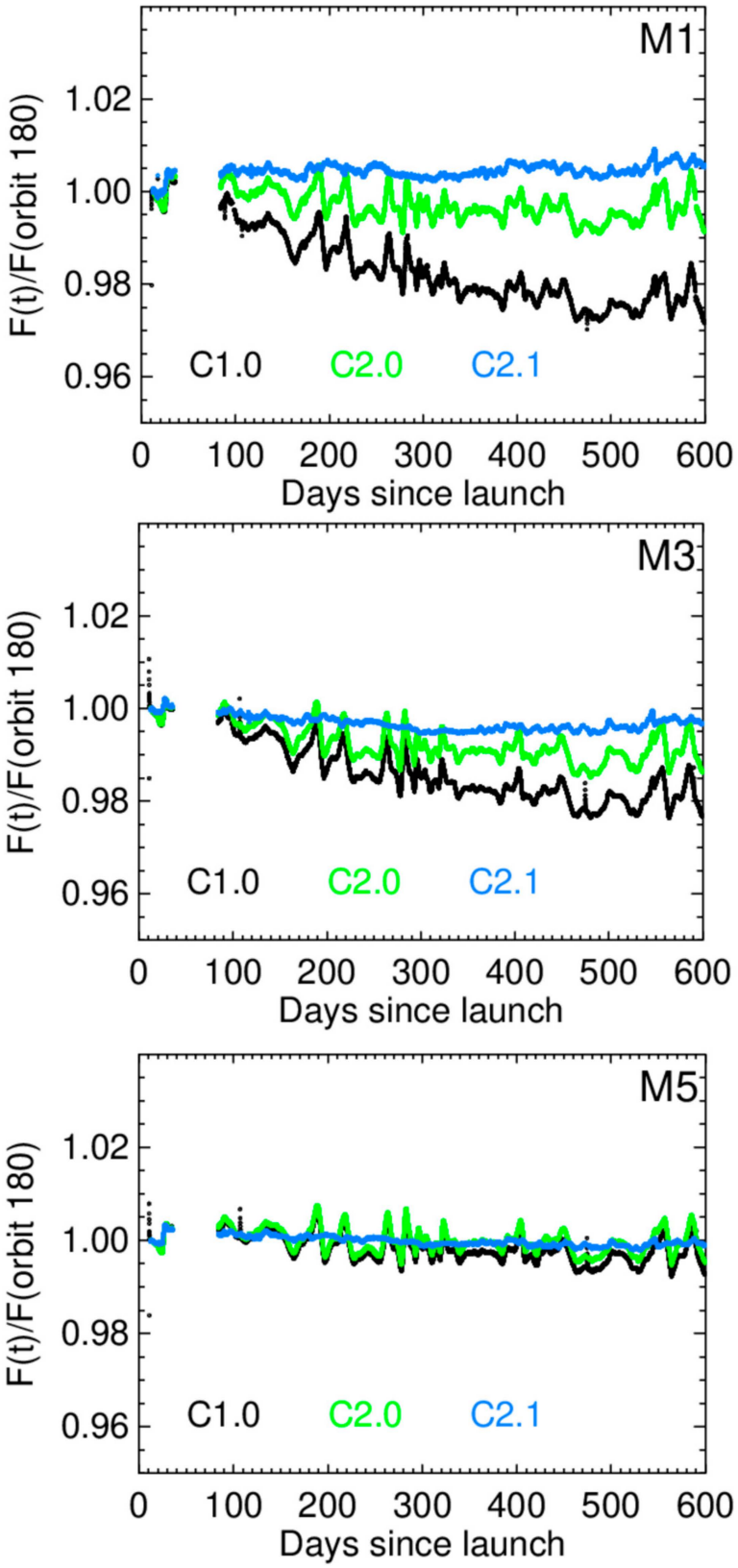

Figure 14. The N21 VIIRS F-factor trend comparison for Collections 1.0, 2.0, and 2.1 for bands M1, M3, and M5.

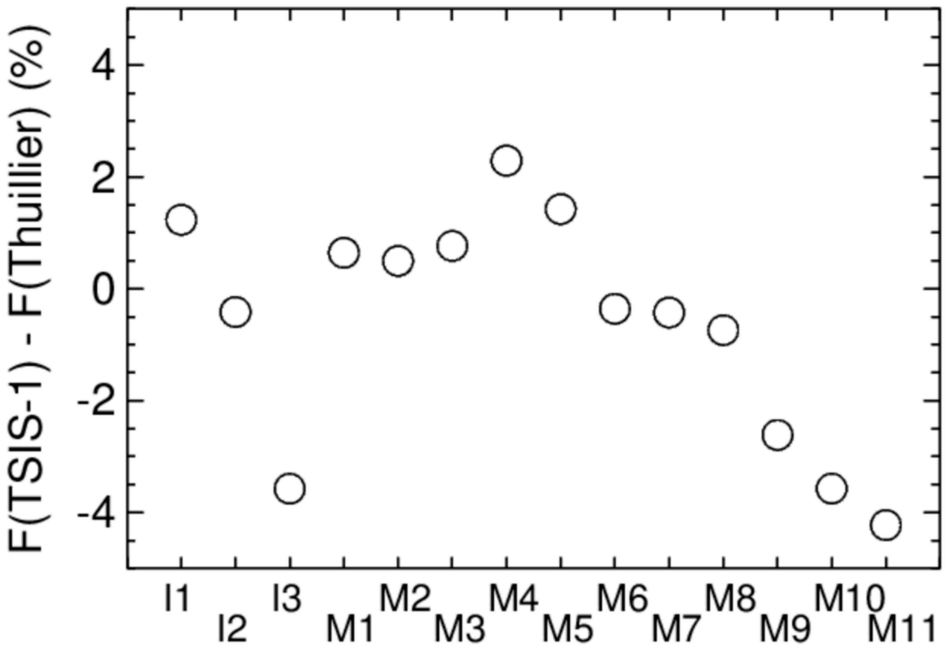

Figure 15. The N21 VIIRS F-factor difference between using the TSIS-1 and the Thuillier solar spectral powers.

The spectral reflectance from the Libya 4 site is from the cloud-free nadir views of a 32-pixel-by-32-pixel area centered at a [latitude, longitude] of [28.55°, 23.39°]. Contrary to the overall upward reflectance trend from the DCC scenes, on a yearly basis, the reflectance from the Libya 4 site stays nearly constant, as shown in Figure 17 (The undulations within a year are considered as the measurement errors.). The figure does not show results for bands M6 and M9 because of detector saturation and photon absorption from the atmospheric water vapor, respectively.

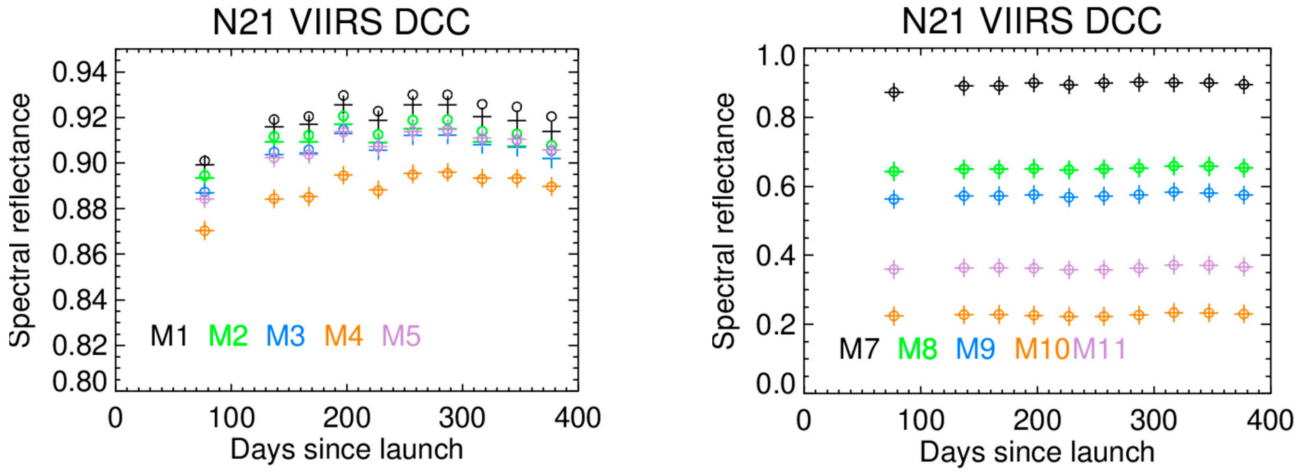

Figure 16. The DCC Collection 2.1 Level 1B spectral reflectance (circles) retrieved by using the N21 VIIRS RSB moderate-resolution bands from the eastern Indian and western Pacific Oceans (20°S–20°N and 95°E–175°E), except band M6 because of saturation. Each data point is from mode reflectance averaged across the detectors in each of the bands over 30 days, over a large telescope scanning angular range around nadir. Collection 2.1 reflectance is obtained from Collection 2.0, by multiplying the F-factor ratio of C2.1 to C2.0. The spectral reflectance for Collection 2.0 is represented by the plus symbols.

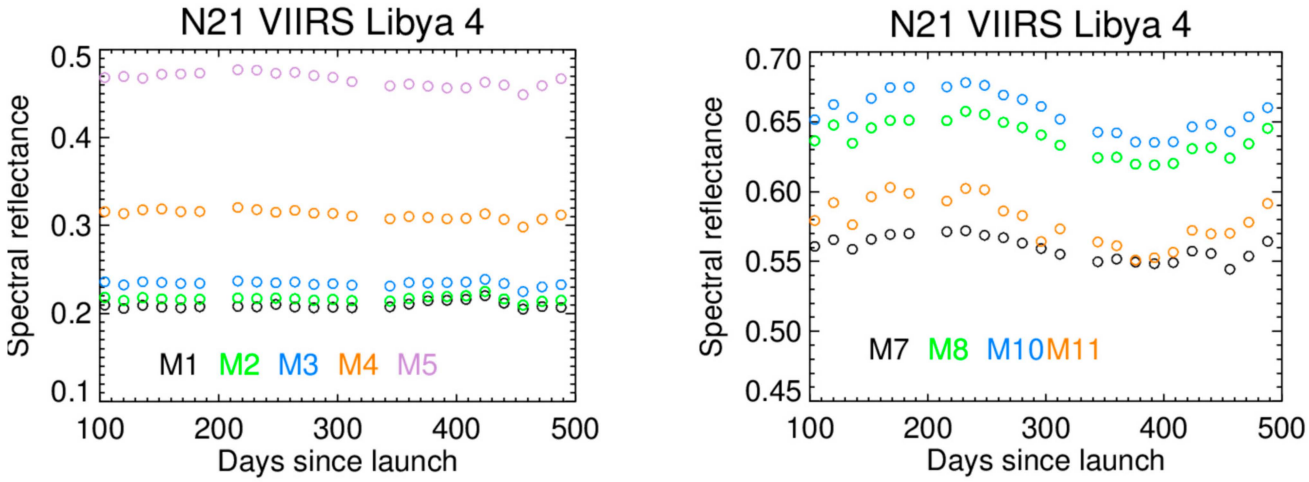

Figure 17. The Libya 4 Collection 2.1 Level 1B spectral reflectance retrieved from the N21 VIIRS RSB moderate-resolution bands, except bands M6 and M9 because of saturation and atmospheric water vapor photon absorption, respectively, averaged across the 16 detectors in each of the bands, from nadir view. Collection 2.1 reflectance is obtained from Collection 2.0, by multiplying the F-factor ratio of C2.1 to C2.0.

5. Striping Assessment and Mitigation

We assess the N21 VIIRS Collection 2.0 RSB L1B TOA spectral reflectance striping, using scenes of DCC, Libya 4, the Moon, and the global view. The global-view data are from two-orbit daytime L1B granules. The global-view scenes are non-uniform and thus allow us to assess striping at a range of radiance levels. The major striping issues are for bands M1-M3 with the striping magnitude at the time of this writing across the 16 detectors close to or larger than 1%. For the other VisNIR bands, a smaller amount, nearly time-independent striping is seen. For the SWIR bands, the striping magnitudes are small, no larger than 0.6%. Here, we mitigate the VisNIR band striping only.

For bands M1-M3, the magnitude of striping increases in time, as shown in Figure 18, signaling the effect of the positional dependence of the SD BRDF on-orbit change factor, the H-factor. The amount of solar exposure on the SD surface is non-uniform, as revealed for the SNPP and N20 VIIRS [52,53]. As a result, the rate of temporal change in the H-factor is SD-position-dependent. Because the detectors in a VIIRS band do not see the same area of the SD, the H-factors for the detectors differ. Figure 18 reveals that the H-factor SD positional dependence strength is weaker at a longer wavelength, seen for the SNPP and N20 VIIRS SDs as well. As we did for the SNPP and N20 VIIRS, we use the same model for the N21 VIIRS H-factor SD positional dependence, with the SD position measured by the detector index in a band:

$$\begin{aligned} &H_{\mathrm{RTA}}(\lambda_{\mathrm{B}}, d) \\ &= H_{\mathrm{RTA}}\left(\lambda_{\mathrm{B}},\ \phi_{\mathrm{V,SD}} = 35.5^{\circ}\right) \times [1 + c_{d,1}(d - d_{\mathrm{mid}}) + c_{d,2}(d - d_{\mathrm{mid}}) \times (1 - H_{\mathrm{RTA}}(\lambda_{\mathrm{B}}, \phi_{\mathrm{V,SD}} = 35.5^{\circ}))], \end{aligned} \tag{22}$$

where $H_{\mathrm{RTA}}\left(\lambda_{\mathrm{B}}, \phi_{\mathrm{V,SD}} = 35.5^{\circ}\right)$ is assumed to be the H-factor (RTA SD view) for an SD area viewed by a detector with an index of d_{mid}, the center detector in the detector array, and d is the detector index. For the M-bands, d ranges from 0 to 15 and d_{mid} is 7.5. $c_{d,1}$ and $c_{d,2}$ are two model parameters to be determined from a least-squares regression to the striping assessment results. Equation (22) is based on the same assumptions as those for Equation (7).

The TOA spectral reflectance, ρ_{EV}, retrieved with $H_{RTA}(\lambda_B, \phi_{V,SD} = 35.5°)$ (no SD positional dependence) but not $H_{RTA}(\lambda_B, d)$ (with SD positional dependence) has striping. The expected spectral reflectance across the two end detectors for an M-band is modeled as

$$\frac{\rho_{EV}(d=0) - \rho_{EV}(d=15)}{\langle \rho_{EV}(d) \rangle} = 15c_{d,1} + 15c_{d,2}\left(1 - H_{RTA}\left(\lambda_B, \phi_{V,SD} = 35.5°\right)\right). \quad (23)$$

The reflectance difference between the two end detectors is obtained from a linear least-squares regression to the reflectance for the 16 detectors. We perform a least-squares regression to fit Equation (23) to the observed striping and find that $c_{d,1}$ are 0.00022 ± 0.00004, 0.00021 ± 0.00005, and 0.00015 ± 0.00003 for bands M1, M2, and M3, respectively, indicating that the $c_{d,1}$ for these three bands are statistically the same. We use the mean of $c_{d,1}$, 0.00019, from bands M1-M3, for all the VisNIR bands as we did for the N20 VIIRS [53]. A non-zero $c_{d,1}$ may mean that the prelaunch BRDF has an SD positional dependence not tabulated into the lookup table. A $c_{d,1}$ value of 0.00019 means that across the 16 M-band detectors, the prelaunch BRDF has a 0.29% bias which is very close to the bias found for the N20 VIIRS SD prelaunch BRDF [53]. For bands M1-M3, $c_{d,2}$ are found to be 0.0049 ± 0.0003, 0.0043 ± 0.0005, and 0.0046 ± 0.0005, respectively, indicating that the $c_{d,2}$ for bands M1-M3 are also statistically the same.

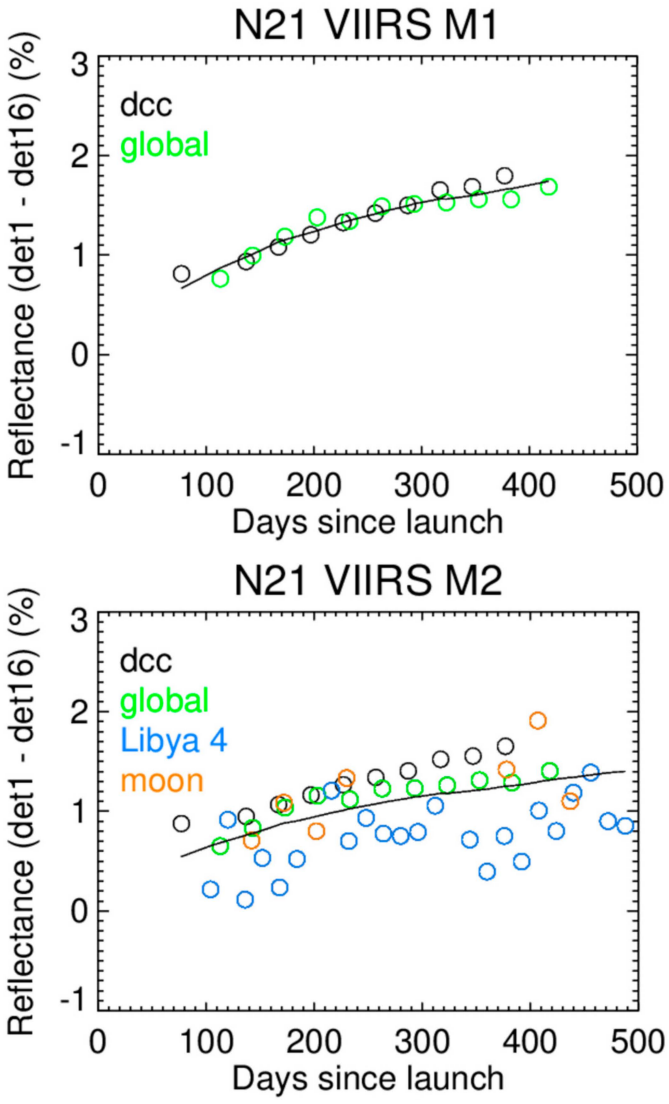

Figure 18. *Cont.*

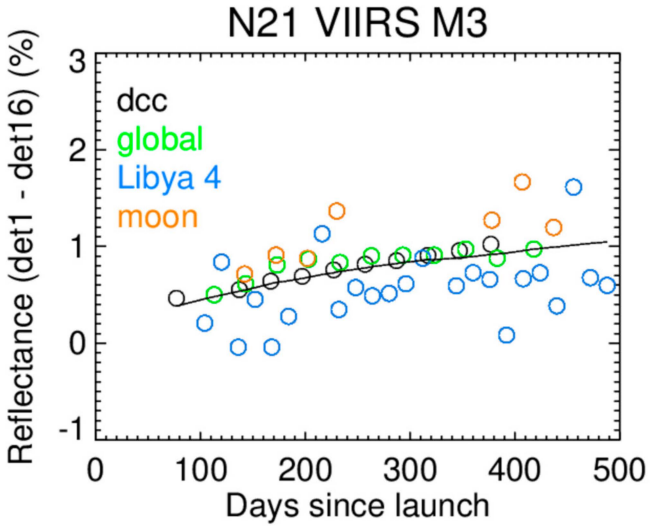

Figure 18. Retrieved N21 VIIRS Collection 2.0 Earth-view Level 1B spectral reflectance (circles) striping for bands M1–M3 (top to bottom) between the end detectors obtained from a linear fit to the reflectance from the 16 detectors in each of the bands, without applying the solar diffuser BRDF on-orbit change factor SD positional dependence. The solid lines are the modeled reflectance for the respective bands (see Equation (23)).

After we find the H-factor SD positional dependence coefficients, $c_{d,1}$ and $c_{d,2}$, we use Equation (22) to recalculate the detector gain correction factor and the F-factor and recompute the L1B reflectance. The unexpected striping in the original L1B Earth-view reflectance images is significantly reduced. As an example, in Figure 19 we compare the L1B band M1 reflectance images of the Libya 4 site, with (image on the right) and without (image on the left) applying the H-factor SD positional dependence. Figure 19 reveals that after applying the H-factor SD positional dependence, the original large striping becomes nearly invisible. Beginning in Collection 2.1, the VisNIR striping improvement has been applied for the mission.

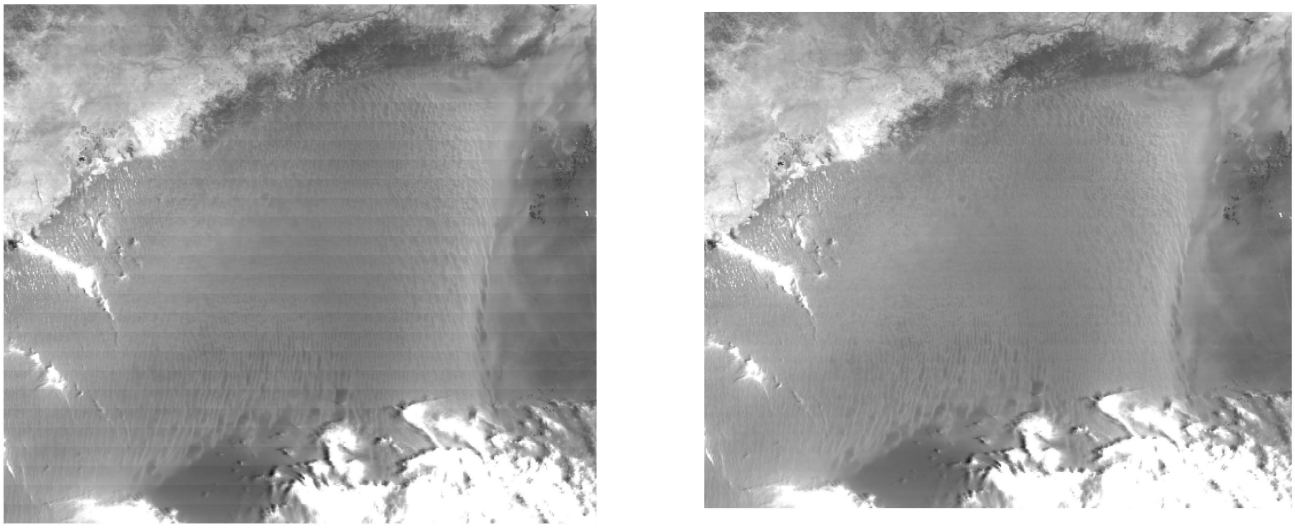

Figure 19. The Libya 4 Level 1B reflectance retrieved from the N21 VIIRS Collection 2.0 L1B band M1's 16 detectors on 30 May 2024, before (**left**) and after (**right**) applying the solar diffuser BRDF on-orbit change factor SD positional dependence (see Equation (22)).

6. L1B Reflectance Factor Uncertainty Estimate: SNR and Bias

The direct readout from a NASA VIIRS L1B product granule for the RSBs is the TOA spectral reflectance factor (or the spectral radiance), defined as the reflectance times the cosine of the angle between the solar and Earth surface normal vectors, $\theta_{\mathrm{EARTH-SUN}}$,

$$\cos\theta_{\mathrm{EARTH-SUN}}\rho_{\mathrm{EV}} = \frac{4\pi^2 F \sum_{i=0}^{2} c_i dn_{\mathrm{EV}}^i \times d_{\mathrm{VIIRS-SUN}}^2 \times \int_0^\infty \mathrm{RSR}(\lambda,t,d)d\lambda}{\mathrm{RVS}(\lambda_{\mathrm{B}},\theta_{\mathrm{EV}}) \times \int_0^\infty \mathrm{RSR}(\lambda,t,d)\Phi_{\mathrm{SUN}}(\lambda,t)d\lambda}, \quad (24)$$

where dn_{EV} is the dark-subtracted detector digital number for the Earth pixel, and θ_{EV} denotes the RTA Earth-view scan angle. Replacing F in Equation (24) with F from Equation (3), the relative variance of the reflectance factor is calculated by

$$\frac{var(\cos\theta_{\mathrm{EARTH-SUN}}*\rho_{\mathrm{EV}})}{(\cos\theta_{\mathrm{EARTH-SUN}}*\rho_{\mathrm{EV}})^2} = \frac{var(dn_{\mathrm{EV}})}{(dn_{\mathrm{EV}})^2} + \frac{var\left(\frac{\mathrm{RVS}(\lambda_{\mathrm{B}},\theta_{\mathrm{SD}})}{\mathrm{RVS}(\lambda_{\mathrm{B}},\theta_{\mathrm{EV}})}\right)}{\left(\frac{\mathrm{RVS}(\lambda_{\mathrm{B}},\theta_{\mathrm{SD}})}{\mathrm{RVS}(\lambda_{\mathrm{B}},\theta_{\mathrm{EV}})}\right)^2} + \frac{var(\sin(\phi_{\mathrm{V,SD}}))}{(\sin(\phi_{\mathrm{V,SD}}))^2} + \frac{var\left(\tau_{\mathrm{SD}}\mathrm{BRDF}_{\mathrm{RTA}}\left(\lambda_{\mathrm{B}},\, t{=}0,\vec{\phi}(t)\right)\right)}{\left(\tau_{\mathrm{SD}}\mathrm{BRDF}_{\mathrm{RTA}}\left(\lambda_{\mathrm{B}},\, t{=}0,\vec{\phi}(t)\right)\right)^2} +$$
$$var(c_{2,1}) \times (dn_{\mathrm{EV}} - dn_{\mathrm{SD}})^2 + \frac{var(H_{\mathrm{RTA}})}{(H_{\mathrm{RTA}})^2}, \quad (25)$$

where $c_{2,1}$ is the ratio of c_2 to c_1. To arrive at Equation (25), we use the properties that c_0 is set to be zero for the current and prior NASA N21 VIIRS RSB L1B products, and the solar spectral power errors in the F-factor calculation and the denominator on the right side of Equation (24) are canceled. dn_{SD} in the per-RTA-scan F-factor calculation is the average over 48 and 96 frames for the M- and I-bands, respectively. Further, the F-factor used in the L1B reflectance retrieval is an average: The per-scan F-factors are averaged on a satellite orbit, and then, the per-orbit F-factors are fitted to a quadratic polynomial in time over a large number of orbits. As a result, the relative variance of dn_{SD} is less than 0.1% and is ignored. The temperatures of the focal plane and electronics at the SD and Earth observation times may not be the same. But the temperature difference's impact on the F-factor is negligibly small because c_1 only weakly depends on the temperatures. Finally, the RSB detector RSR center wavelength may have an error of about 0.1 nm [54]. As a result, the RSR-solar spectral power-H-factor wavelength integral may have the largest error for band M1 (shortest band center wavelength among the RSBs) with the slope of the H-factor with respect to the wavelength being about 0.26% per nm currently, meaning that a 0.1 nm error in the RSR center wavelength results in a 0.026% error in the F-factor, a negligible small number.

The variance of dn_{EV} is due to noise as well as digitization, mainly from the detector's Earth-view raw digital number. The background digital number is from the reading over the SV, an average over 48 and 96 frames for the M- and I-bands, respectively. The ratio of dn_{EV} to its standard deviation is defined as the signal-to-noise ratio (SNR). The required SNRs at the typical spectral radiance (L_{typ}) levels are listed in Table 1. Since the N21 launch, the N21 VIIRS RSB SNRs at L_{typ} have all been above the requirements with large margins, and the SNRs have also been stable over time, as shown in Figure 20. To assist with finding the SNR at L_{typ}, the measured SNRs are obtained from the RSB SD views over a large range of solar angles to sense a large range of spectral radiance [55]. Note that the SD view raw digital number, DN_{SD}, is in 14-bit, whereas the EV view raw digital number, DN_{EV}, is in 12-bit. In finding the SNR for the Earth view, we account for the extra uncertainty brought by the digitization. In finding the SNR, we take care of the scan frame aggregation effect [41]. (The real time calculation of the SNR is performed through $var(dn_{\mathrm{EV}}) = k_0 + k_1 dn_{\mathrm{EV}}$ where k_0 and k_1 are determined offline through the SD observation and tabulated into lookup tables.)

The RVS is close to unity and so is the ratio in the denominator in the second term on the right side of Equation (25). The prelaunch-determined RVS is from a least-squares fit

of a quadratic polynomial in the angle of incidence (AOI) for the HAM to the measured values [56]:

$$RVS(AOI) = a + b * (AOI - AOI_{\text{ref}}) + c * (AOI - AOI_{\text{ref}})^2. \quad (26)$$

where AOI_{ref} is a fixed reference angle. Note that RVS is close to one and so is a in Equation (26). The uncertainty of the measurements leads to the uncertainty of the fit-determined quadratic polynomial coefficients. By using the fact that a in Equation (26) is close to unity, the variance of the ratio of $\text{RVS}(\lambda_B, \theta_{SD})$ to $\text{RVS}(\lambda_B, \theta_{EV})$ is computed by

$$var\left(\frac{\text{RVS}(\lambda_B, \theta_{SD})}{\text{RVS}(\lambda_B, \theta_{EV})}\right) = var(b/a) \times (AOI_{SD} - AOI_{EV})^2. \quad (27)$$

The RVS standard deviations for the N21 VIIRS RSBs can be found in the literature [10,56]. The largest RVS standard deviation is 0.07% for band M1 at an AOI of 28.6° which is 31.87° away from an AOI_{SD} of 60.47° [10,57]. For the nadir view, AOI_{EV} is 36.08° [57]. For all other RSBs, the largest RVS standard deviations are no larger than 0.04%. The RVS model, Equation (26), assumes that the HAM's reflectivity is independent of the azimuth angle. The azimuth angle dependence may occur, and in this case, Equation (26) is invalid. Fortunately, for the N21 VIIRS HAM, we have not found any RVS azimuth angle dependence, suggested by the near unity of the lunar irradiance ratio of HAM side A to HAM side B.

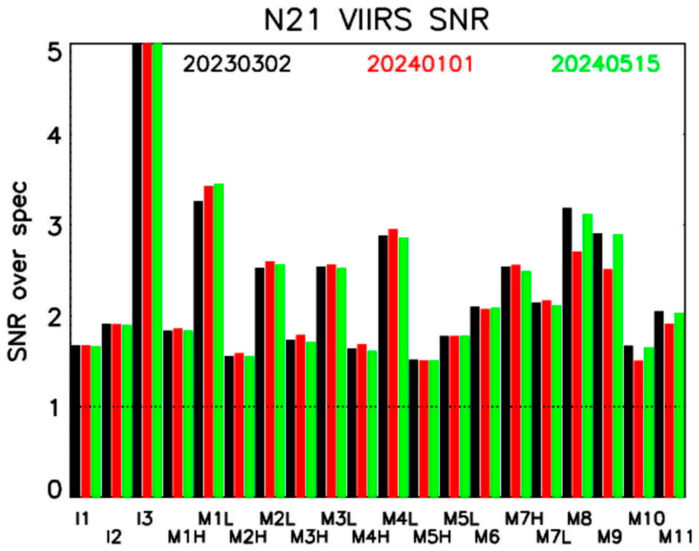

Figure 20. The N21 VIIRS RSB signal-to-noise ratios at the respective specified typical spectral radiances for a single frame from the Earth view divided by the respective required signal-to-noise ratios, on 2 March 2023 (black), 1 January 2024 (red), and 15 May 2024 (green).

The error in $\sin(\phi_{V,SD})$ is due to the SD orientation uncertainty, assessed during prelaunch tests. At the center of the calibration sweet spot, $\sin(\phi_{V,SD})$ has an uncertainty of 0.33% [10].

The SD screen transmittance, τ_{SD}, and the SD BRDF for the RTA SD view, $\text{BRDF}_{RTA}\left(\lambda_B,\ t = 0, \vec{\phi}(t)\right)$, were measured separately in the laboratory before the satellite launch. The relative standard deviations of τ_{SD} and $\text{BRDF}_{RTA}\left(\lambda_B,\ t = 0, \vec{\phi}(t)\right)$ are 0.24% and 0.91%, respectively [10]. Additionally, because of the large time span between the prelaunch measurement and the satellite launch, the SD BRDF may change, and we assign an extra standard deviation of 0.5% for the BRDF to account for this possible change. Adding together the uncertainty contributors associated with τ_{SD} and $\text{BRDF}_{RTA}\left(\lambda_B,\ t = 0, \vec{\phi}(t)\right)$, the relative standard deviation of $\tau_{SD}\text{BRDF}_{RTA}\left(\lambda_B,\ t = 0, \vec{\phi}(t)\right)$

is 1.066%. As mentioned earlier, the prelaunch BRDF measurements were performed at six wavelengths up to 1.63 μm [33]. At band M11, center wavelength of 2.25 μm, the BRDF s found from extrapolation. The extrapolation error may be large; the reason that we increase the prelaunch BRDF at 2.25 μm by 6.1% is so that the lunar irradiances from the N20 and N21 VIIRS band M11 match. The standard deviation of the BRDF extrapolation is estimated to be 1.7% [10].

The uncertainty contribution from $c_{2,1}$ to the L1B Earth-view spectral reflectance factor is coupled with the difference in the dark-subtracted dn at the SD and the Earth views. The standard deviation of $c_{2,1}$ is in the range of high 10^{-7} to about 2×10^{-5} [DN^{-1}], measured at prelaunch time. If $dn_{EV} - dn_{SD}$ is large, for example, 3000 [DN], then $std(c_{2,1}) \times \lceil dn_{EV} - dn_{SD} \rceil$ can be as large as 0.06, namely, 6%, a very large error. However, the dn at the typical spectral radiance, dn_{typ}, is often very close to dn_{SD}; this is the purpose of the SD screen. Hence, at L_{typ}, the uncertainty contribution from $c_{2,1}$ is very small generally.

The uncertainty of H_{RTA} comes from H^{M}_{SDSM} and the ratio of $F(B,t;SNPP)$ to $F\left[H^{M}_{SDSM}(B,t;SNPP)\right]$. The standard deviation of H^{M}_{SDSM} mainly comes from the uncertainty associated with the extrapolation to the start of the mission. As shown in Figure 8, the extrapolation slope is highly affected by the screen function accuracy. Here, we estimate that H^{M}_{SDSM} has a 0.3% standard deviation. The uncertainty of the ratio of $F(B,t;SNPP)$ to $F\left[H^{M}_{SDSM}(B,t;SNPP)\right]$ for the VisNIR bands may be estimated from the pseudo-invariant sites' L1B reflectance temporal trends. From the Libya 4 reflectance trends shown in Figure 17, the ratio is quite accurate and may have a 0.15% per year error. Here, we use 0.15% per year as the upper limit for the uncertainty of the ratio. Note that the Libya 4 spectral radiance is not strong enough, so the RSB dual-gain bands are mainly in the high-gain stage. The DCC reflectance trends may not indicate that the ratio of $F(B,t;SNPP)$ to $F\left[H^{M}_{SDSM}(B,t;SNPP)\right]$ is inaccurate because of the large yearly undulation and relatively short time span (see Figure 16).

Adding all uncertainty contributions on the right side of Equation (25), as of 15 May 2024, the relative standard deviations of the L1B reflectance factors for the N21 VIIRS RSBs are estimated to be all less than 1.5%, except band M11, as shown in Figure 21. The uncertainty for band M11 is much higher at 2.2% because of the large uncertainty of the BRDF extrapolation at 2.25 μm. We realize that our reflectance factor uncertainty analysis may not account for the calibration uncertainty associated with the F-factor determination from using the sunlit SD for the dual-gain bands at the low-gain stage because the SD-provided spectral radiance is below the design detection range by at least 25%.

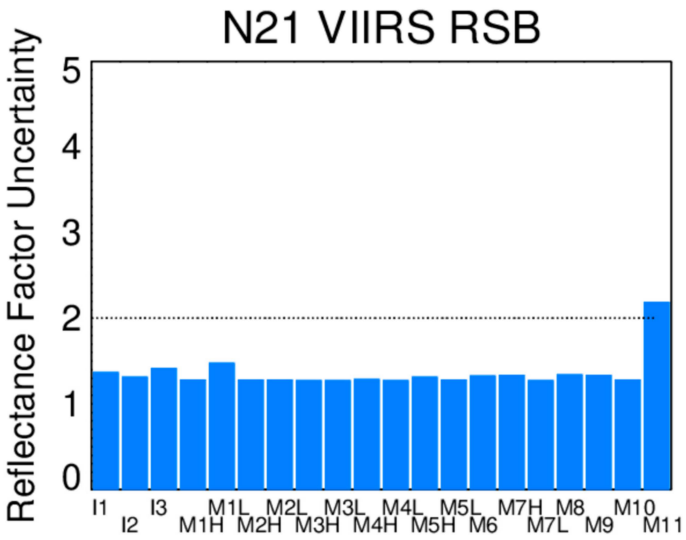

Figure 21. The estimated relative standard deviations for the N21 VIIRS RSBs at the respective specified spectral radiances on 15 May 2024. The dots indicate the 2% requirement.

7. Conclusions

Based on the prelaunch calibration results, we have performed on-orbit radiometric calibration for the N21 VIIRS reflective solar bands using the onboard sunlit solar diffuser. In the most recent calibration version of the NASA N21 VIIRS product Collection 2.1, we use the TSIS-1 solar spectral power to retrieve the correction factor to the detector digital number quadratic polynomial to retrieve a scene's spectral radiance, the F-factor. To calculate the F-factor, we use the SD BRDF on-orbit change factor, the H-factor, determined by the SDSM detectors, without SDSM detector RSR deconvolution. The F-factor was then multiplied by a factor obtained from the SNPP VIIRS RSBs: the ratio of the F-factor calculated with the H-factor for the telescope SD view to the F-factor calculated with the SDSM-measured H-factor without RSR deconvolution. We have improved the SDSM screen's transmittance function accuracy, using the calibration data collected at both the yaw maneuver and a small portion of the regular times. The products of the SD screen transmittance and the BRDF at the start of the mission for both the RTA and SDSM SD views have also been improved by applying the angular dependency of the H-factor. The improved screen functions not only significantly reduce the unexpected undulations in the retrieved H- and F-factors but also improve the absolute accuracy of the two factors because of improved accuracy of the H-factor temporal trend which is extrapolated to the start of the mission. Further, we have analyzed the L1B Earth-view reflectance striping in Collection 2.0 and found that, at the time of this writing, the largest, unexpected striping of about 1% or larger than 1% occurs only for bands M1–M3. The striping for bands M1–M3 is due to the uneven solar exposure on the SD surface, and consequently, the H-factor depends on the SD surface position. Applying a correction based on the H-factor SD positional dependence originally developed for the SNPP VIIRS, we have essentially removed the striping in Collection 2.1. We have found that the detector signal-to-noise ratios have been stable over time and above the requirements with large margins. Improving upon the previous N21 VIIRS collections, we have used a wavelength power law to extrapolate the SDSM-measured H-factors to the SWIR wavelengths. Finally, we have analyzed the L1B reflectance factor uncertainty and estimated that the uncertainty is below 1.5% for all the RSBs, better than the 2% requirement, except band M11 whose uncertainty is 2.2%.

Author Contributions: Conceptualization, N.L., A.A. and X.X.; methodology, N.L., Q.M., S.L., T.C. and K.T.; data analysis, N.L., S.L., Q.M., K.T., T.C. and A.A.; writing—original draft preparation, N.L.; writing—review, all authors; figures and tables, N.L., K.T., A.A., S.L. and Q.M. All authors have read and agreed to the published version of the manuscript.

Funding: This research is supported by the NASA SNPP project and the VIIRS SDR Calibration Support from NOAA SNPP/JPSS Program.

Data Availability Statement: The original contributions presented in the study are included in the article, further inquiries can be directed to the corresponding author.

Acknowledgments: We would like to thank Kwofu Chiang, Truman Wilson, Xu Geng, and Aisheng Wu of the NASA VIIRS Characterization Support Team for useful communications and for providing the N21 VIIRS L1B granules and Kwofu Chiang for review comments.

Conflicts of Interest: Authors Ning Lei, Kevin Twedt, Sherry Li, Tiejun Chang, Qiaozhen Mu and Amit Angal are employed by the company Science Systems and Applications Inc. The remaining authors declare that the research was conducted in the absence of any commercial or financial relationships that could be construed as a potential conflict of interest.

Appendix A. Definitions of the VIIRS SDSM Screen and VIIRS Coordinate Systems

In the VIIRS SDSM screen coordinate system, the solar declination and azimuth angles are calculated as $\phi_{\mathrm{V,SDSM}} = \arcsin(z/r)$ and $\phi_{\mathrm{H,SDSM}} = \arctan(-y/x)$ where $r = \sqrt{x^2 + y^2 + z^2}$.

The VIIRS coordinate system is defined as follows: The x axis is along the telescope rotation axis, and the z axis is from the telescope to the EV port center. The x, y, and z axes

follow the right-hand rule. The solar angles are calculated as $\phi_{\mathrm{H,VIIRS}} = -\arctan(y/x)$ and $\phi_{\mathrm{V,VIIRS}} = \arctan(z/x)$.

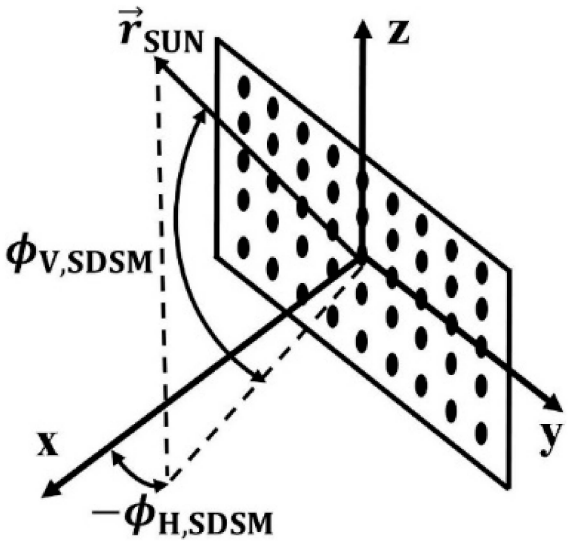

Figure A1. A schematic diagram showing the definition of the VIIRS SDSM screen coordinate system. The plate with dots indicates the SDSM screen, and the dots indicate the through holes on the screen. The x axis is along the SDSM screen normal vector, and the y axis is along the long dimension of the screen. $\vec{r}_{\mathrm{SUN}}$ is the solar vector.

Appendix B

Table A1. Acronym definitions.

Acronyms	Definitions
AOI	Angle of incidence with respect to the half-angle mirror surface
AOI_{SD}	Angle of incidence with respect to the half-angle mirror surface when the telescope aims at the solar diffuser
AOI_{EV}	Angle of incidence with respect to the half-angle mirror surface when the telescope aims at the Earth
BRDF	Bidirectional reflectance distribution function
$\mathrm{BRDF}_{\mathrm{RTA}}$	Bidirectional reflectance distribution function for the telescope solar diffuser view
$\mathrm{BRDF}_{\mathrm{SDSM}}$	Bidirectional reflectance distribution function for the solar diffuser stability monitor solar diffuser view
DC	Solar diffuser stability monitor detector count without background subtraction
dc	Solar diffuser stability monitor detector count with background subtraction
dc_{SD}	Background-subtracted digital count for the solar diffuser stability monitor detector solar diffuser view
dc_{SUN}	Background-subtracted digital count for the solar diffuser stability monitor detector Sun view
$dc_{\mathrm{SUN,adj}}$	Background-subtracted digital count for the solar diffuser stability monitor detector Sun view with temperature impact removed
$dc_{\mathrm{sun,norm}}$	Background-subtracted digital count for the solar diffuser stability monitor detector Sun view with temperature impact, distance between the Sun and the VIIRS, and the SDSM screen transmittance impacts removed, defined by Equation (15)

Table A1. *Cont.*

Acronyms	Definitions
DCC	Deep convective cloud
DN	Reflective solar band detector digital number without background subtraction
dn	Reflective solar band detector digital number with background subtracted
$d_{\mathrm{VIIRS-SUN}}$	Distance between the VIIRS and the Sun
F-factor	A correction factor for the scene spectral radiance calculated by using the dn quadratic polynomial, defined by Equation (1)
F_{MOON}	F-factor derived from lunar views
HAM	Half-angle mirror which reflects sunlight collected by the telescope to the aft optics
H_{RTA}	Solar diffuser BRDF on-orbit change factor for the telescope solar diffuser view
H_{SDSM}	True solar diffuser BRDF on-orbit change factor for the solar diffuser stability monitor solar diffuser view, typically found by deconvolving $H^{\mathrm{MEA}}_{\mathrm{SDSM}}$ defined below
$H^{\mathrm{M}}_{\mathrm{SDSM}}$	Measured solar diffuser BRDF on-orbit change factor for the solar diffuser stability monitor solar diffuser view without deconvolution
$\overline{I_{\mathrm{ROLO}}}$	Spectral irradiance for the Moon calculated from the Robotic Lunar Observatory model developed by the US Geological Survey, weighted by the relative spectral response function of the band
I-band	Imaging band: nominal nadir resolution of 375 m
JPSS	Joint Polar Satellite System (between NASA and NOAA)
L	Scene spectral radiance
L_{SD}	Spectral radiance provided by the solar diffuser for the telescope solar diffuser view
L_{typ}	Typical Earth-view spectral radiance for a band
L1B	Level-1 B: geometrically and radiometrically calibrated Earth-view spectral radiance and reflectance
LUT	Lookup table: a table which the L1B code reads to produce spectral radiance and reflectance
λ_B	Band central wavelength for a band denoted by B
λ_d	Band central wavelength for a solar diffuser stability monitor detector with its index denoted by d
M-band	Moderate-resolution band: nominal nadir resolution of 750 m
$\mathrm{N_{agg}}$	Number of frames to aggregate for forming a pixel in Level-1B products
$\mathrm{N_{SCAN}}$	Number of scans that have the entire lunar image captured by the detector array in a band
N21	NOAA-21
Ω_{B}	VIIRS RSB detector object view solid angle before aggregation
$\vec{\phi}$	Solar angle
ϕ_{H}	Solar azimuth angle with respect to the SD surface normal vector
$\phi_{\mathrm{H,SDSM}}$	Solar azimuth angle with respect to the SDSM screen normal vector in the SDSM screen coordinate system defined in Appendix A
Φ_{SUN}	Solar spectral power
$\phi_{\mathrm{V,SD}}$	Angle between the solar vector and the SD surface plane
ρ_{EV}	Top-of-the-atmosphere spectral reflectance

Table A1. *Cont.*

Acronyms	Definitions
ROLO	Robotic Lunar Observatory model developed by the US Geological Survey
RSB	Reflective solar band
RSR	Relative spectral response function of a band
RTA	Rotating telescope assembly: the VIIRS telescope, the first component in the VIIRS optical path
SD	Solar diffuser
SDSM	Solar diffuser stability monitor
SNPP	Suomi National Polar-orbiting Partnership
SV	Space view port, providing a dark scene
SWIR	Shortwave infrared
$\tau^{R}_{SDSM,eff}$	SDSM screen's relative effective transmittance
$\tau^{R}_{SD,eff}BRDF_{SDSM}$	Product of the solar diffuser screen's relative effective transmittance and the BRDF for the SDSM solar diffuser view
$\tau^{R}_{SD}BRDF_{RTA}$	Relative product of the solar diffuser screen transmittance and the BRDF for the telescope solar diffuser view
$\tau_{SD}BRDF_{RTA}$	Product of the solar diffuser screen transmittance and the BRDF for the telescope solar diffuser view
t_{mid}	Time associated with a data point that is about the middle in a data time sequence
$\theta_{EARTH-SUN}$	Angle between the solar vector and Earth surface normal vector
θ_{EV}	Angle of incidence with respect to the half-angle mirror when the telescope aims at the Earth
θ_{SD}	Angle of incidence with respect to the half-angle mirror when the telescope aims at the solar diffuser
$T_{bulkhead}$	Bulkhead temperature in Kelvin
TOA	Top-of-the-atmosphere
VIIRS	Visible Infrared Imaging Radiometer Suite

Appendix C

Table A2. Values of α_{RTA} and their estimated standard deviations for the SNPP VIIRS RSBs (used for N21 VIIRS RSBs as well).

Band	α_{RTA}	std (α_{RTA})	λB (μm)
I1	0.20	0.12	0.638
I2	0.25	0.42	0.862
I3	0.0	5.65	1.601
M1	0.23	0.03	0.411
M2	0.17	0.04	0.443
M3	0.13	0.05	0.486
M4	0.10	0.07	0.551
M5	0.11	0.16	0.671
M6	0.14	0.25	0.745
M7	0.18	0.42	0.862
M8	0.0	1.88	1.238
M9	0.0	2.94	1.375
M10	0.0	5.63	1.601
M11	0.0	23.4	2.257

References

1. Wolfe, R.; Lin, G.; Nishihama, M.; Tewari, K.; Tilton, J.; Isaacman, A. Suomi NPP VIIRS prelaunch and on-orbit geometric calibration and characterization. *J. Geophy. Res. Atmos.* **2013**, *118*, 11508–11521. [CrossRef]
2. Lin, G.; Wolfe, R.; Tilton, J. Trending of SNPP ephemeris and its implications on VIIRS geometric performance. *Proc. SPIE* **2016**, *9972*, 485–495. [CrossRef]
3. Schueler, C.; Clement, J.; Ardanuy, P.; Welsch, C.; De Luccia, F.; Swenson, H. NPOESS VIIRS sensor design overview. *Proc. SPIE* **2012**, *4483*, 11–23. [CrossRef]
4. Murphy, R.; Ardanuy, P.; De Luccia, F.; Clement, J.; Schueler, C. The visible infrared imaging radiometer suite. In *Earth Science Satellite Remote Sensing*; Qu, J., Gao, W., Kafatos, M., Murphy, R., Salomonson, V., Eds.; Springer-Verlag: New York, NY, USA, 2006; Volume 1, pp. 199–223.
5. *Joint Polar Satellite System (JPSS) VIIRS Radiometric Calibration Algorithm Theoretical Basis Document (ATBD)*; NASA Goddard Space Flight Center: Greenbelt, MD, USA, 2013.
6. Cao, C.; Zhang, B.; Shao, X.; Wang, W.; Uprety, S.; Choi, T.; Blonski, S.; Gu, Y.; Bai, Y.; Lin, L.; et al. Mission-Long Recalibrated Science Quality Suomi NPP VIIRS Radiometric Dataset Using Advanced Algorithms for Time Series Studies. *Remote Sens.* **2021**, *13*, 1075. [CrossRef]
7. Zhou, L.; Divakarla, M.; Liu, X.; Layns, A.; Goldberg, M. An Overview of the Science Performances and Calibration/Validation of Joint Polar Satellite System Operational Products. *Remote Sens.* **2019**, *11*, 698. [CrossRef]
8. Oudrari, H.; McIntire, J.; Xiong, X.; Butler, J.; Ji, Q.; Schwarting, T.; Angal, A. An Overall Assessment of JPSS-2 VIIRS Radiometric Performance Based on Pre-Launch Testing. *Remote Sens.* **2018**, *10*, 1921. [CrossRef]
9. Angal, A.; Moyer, D.; Ji, Q.; McIntire, J.; Oudrari, H.; Xiong, X. Prelaunch characterization and performance of JPSS-2 VIIRS reflective solar bands. *Proc. SPIE* **2018**, *10764*, 1076403. [CrossRef]
10. Moyer, D.; Angal, A.; Ji, Q.; McIntire, J.; Xiong, X. JPSS-2 VIIRS Pre-Launch Reflective Solar Band Testing and Performance. *Remote Sens.* **2022**, *14*, 6353. [CrossRef]
11. Lei, N.; Wang, Z.; Xiong, X. On-orbit Radiometric Calibration of Suomi NPP VIIRS Reflective Solar Bands through Observations of a Sunlit Solar Diffuser Panel. *IEEE Trans. Geosci. Remote Sens.* **2015**, *53*, 5983–5990. [CrossRef]
12. Twedt, K.; Lei, N.; Xiong, X.; Angal, A.; Li, S.; Chang, T.; Sun, J. On-Orbit Calibration and Performance of NOAA-20 VIIRS Reflective Solar Bands. *IEEE Trans. Geosci. Remote Sens.* **2022**, *60*, 1001413. [CrossRef]
13. Choi, T.; Cao, C.; Shao, X.; Wang, W. S-NPP VIIRS Lunar Calibrations over 10 Years in Reflective Solar Bands (RSB). *Remote Sens.* **2022**, *14*, 3367. [CrossRef]
14. Choi, T.; Cao, C.; Blonski, S.; Shao, X.; Wang, W. NOAA-20 VIIRS On-orbit Reflective Solar Band Radiometric Calibration Five-Year Update. *IEEE Trans. Geosci. Remote Sens.* **2024**, *62*, 1000610. [CrossRef]
15. Eplee, R.; Turpie, K.; Meister, G.; Patt, F.; Franz, B.; Bailey, S. On-orbit calibration of the Suomi National Polar-Orbiting Partnership Visible Infrared Imaging Radiometer Suite for ocean color applications. *Appl. Opt.* **2015**, *54*, 1984–2006. [CrossRef] [PubMed]
16. Fulbright, J.; Lei, N.; Efremova, B.; Xiong, X. Suomi-NPP VIIRS Solar Diffuser Stability Monitor Performance. *IEEE Trans. Geosci. Remote Sens.* **2016**, *54*, 631–639. [CrossRef]
17. Lei, N. Examining the angular dependence of the SNPP VIIRS Solar Diffuser bidirectional reflectance distribution function degradation factor: I. *VCST Tech. Rep.* **2014**, 2014_006.
18. Lei, N.; Chiang, K.; Xiong, X. Examination of the angular dependence of the SNPP VIIRS solar diffuser BRDF degradation factor. *Proc. SPIE* **2014**, *9218*, 550–562. [CrossRef]
19. Lei, N.; Xiong, X. Impacts of the Angular Dependence of the Solar Diffuser BRDF Degradation Factor on the SNPP VIIRS Reflective Solar Band On-Orbit Radiometric Calibration. *IEEE Trans. Geosci. Remote Sens.* **2017**, *55*, 1537–1543. [CrossRef]
20. Sun, J.; Wang, M. Visible Infrared Imaging Radiometer Suite solar diffuser calibration and its challenges using a solar diffuser stability monitor. *Appl. Opt.* **2014**, *53*, 8571–8584. [CrossRef]
21. Klein, S.; Murgai, V.; Johnson, L. Solar Attenuation Screen Transmittance, Modulation, and Albedo for JPSS J2. *Proc. SPIE* **2019**, *11127*, 61–68. [CrossRef]
22. Valencia, A.; Klein, S.; Murgai, V. Solar Attenuation Screen Transmittance, Modulation, and Albedo for JPSS J3 and J4. *Proc. SPIE* **2020**, *11501*, 115010V. [CrossRef]
23. McIntire, J.; Moyer, D.; Efremova, B.; Oudrari, H.; Xiong, X. On-orbit Characterization of S-NPP VIIRS Transmission Functions. *IEEE Trans. Geosci. Remote Sens.* **2015**, *53*, 2354–2892. [CrossRef]
24. Sun, J.; Chu, M.; Wang, M. On-orbit characterization of the VIIRS solar diffuser and attenuation screens for NOAA-20 using yaw measurements. *Appl. Opt.* **2018**, *57*, 6605–6619. [CrossRef] [PubMed]
25. Sun, J.; Lei, N. JPSS-2 VIIRS Post-Launch Test (PLT) CSE6: Yaw Maneuver Analysis. *VCST Tech. Rep.* **2023**, 2023_028.
26. Lei, N.; Chen, X.; Xiong, X. Determination of the SNPP VIIRS SDSM Screen Relative Transmittance from Both Yaw Maneuver and Regular On-Orbit Data. *IEEE Trans. Geosci. Remote Sens.* **2016**, *54*, 1390–1398. [CrossRef]
27. Lei, N.; Xiong, X. Products of the SNPP VIIRS SD Screen Transmittance and the SD BRDFs from Both Yaw Maneuver and Regular On-orbit Data. *IEEE Trans. Geosci. Remote Sens.* **2017**, *55*, 1975–1987. [CrossRef]
28. Lei, N.; Xiong, X. Determination of NOAA-20 VIIRS screen transmittance functions with both yaw maneuver and regular on-orbit calibration data. *J. Appl. Opt.* **2020**, *59*, 2992–3001. [CrossRef]

29. Xiong, X.; Butler, J.; Chiang, K.; Efremova, B.; Fulbright, J.; Lei, N.; McIntire, J.; Oudrari, H.; Sun, J.; Wang, Z.; et al. VIIRS on-orbit calibration methodology and performance. *J. Geophys. Res. Atmos.* **2014**, *119*, 5065–5078. [CrossRef]
30. Lei, N.; Xiong, X.; Wang, Z.; Li, S.; Twedt, K. SNPP VIIRS RSB on-orbit radiometric calibration algorithms Version 2.0 and the performances, part 1: The algorithms. *J. Appl. Remote Sens.* **2020**, *14*, 047501. [CrossRef]
31. Lei, N.; Twedt, K.; Xiong, X.; Angal, A. Performance of NOAA-20 VIIRS Solar Diffuser and Solar Diffuser Stability Monitor. *IEEE Trans. Geosci. Remote Sens.* **2021**, *59*, 7180–7188. [CrossRef]
32. Wu, A.; Xiong, X.; Cao, C. Assessment of stability of the response versus scan angle for the S-NPP VIIRS reflective solar bands using pseudo-invariant desert and Dome C sites. *Proc. SPIE* **2017**, *10423*, 432–440. [CrossRef]
33. Murgai, V.; Klein, S. Spectralon® Solar Diffuser BRDF Extrapolation to 2.25 microns for JPSS J1, J2 and J3. *Proc. SPIE* **2019**, *11127*, 75–85. [CrossRef]
34. Kieffer, H.H. Photometric Stability of the Lunar Surface. *Icarus* **1997**, *130*, 323–327. [CrossRef]
35. Kieffer, H.H.; Stone, T.C. The Spectral Irradiance of the Moon. *Astron. J.* **2005**, *129*, 2887–2901. [CrossRef]
36. Xiong, X.; Sun, J.; Fulbright, J.; Wang, Z.; Butler, J. Lunar Calibration and Performance for S-NPP VIIRS Reflective Solar Bands. *IEEE Trans. Geosci. Remote Sens.* **2016**, *54*, 1052–1061. [CrossRef]
37. Lei, N.; Xiong, X. Suomi NPP VIIRS Solar Diffuser BRDF Degradation Factor at Short Wave Infrared Band Wavelengths. *IEEE Trans. Geosci. Remote Sens.* **2016**, *54*, 6212–6216. [CrossRef]
38. Lei, N.; Xiong, X.; Li, S.; Twedt, K. SNPP VIIRS solar vector orientation knowledge error revealed by solar diffuser stability monitor sun views. *J. Appl. Remote Sens.* **2024**, *18*, 027502. [CrossRef]
39. Choi, T.; Blonski, S.; Shao, X.; Wang, W. Preliminary assessment of the NOAA-21 VIIRS on-orbit Reflective Solar Band calibration and performance. *Proc. SPIE* **2023**, *12685*, 243–256. [CrossRef]
40. De Luccia, F.; Moyer, D.; Johnson, E.; Rausch, K.; Lei, N.; Chiang, K.; Xiong, X.; Fulbright, J.; Hass, E.; Iona, G. Discovery and characterization of on-orbit degradation of the Visible Infrared Imaging Radiometer Suite (VIIRS) Rotating Telescope Assembly (RTA). *Proc. SPIE* **2012**, *8510*, 477–493. [CrossRef]
41. Lei, N.; Xiong, X.; Wang, Z.; Li, S.; Twedt, K. SNPP VIIRS RSB on-orbit radiometric calibration algorithms Version 2.0 and the performances, part 2: The performances. *J. Appl. Remote Sens.* **2020**, *14*, 047502. [CrossRef]
42. Coddington, O.M.; Richard, E.C.; Harber, D.; Pilewskie, P.; Woods, T.N.; Chance, K.; Liu, X.; Sun, K. The TSIS-1 Hybrid Solar Reference Spectrum. *Geophys. Res. Lett.* **2020**, *48*, e2020GL091709. [CrossRef]
43. Bhatt, R.; Doelling, D.R.; Coddington, O.; Scarino, B.; Gopalan, A.; Haney, C. Quantifying the Impact of Solar Spectra on the Inter-Calibration of Satellite Instruments. *Remote Sens.* **2021**, *13*, 1438. [CrossRef]
44. Kurucz, R. High resolution irradiance spectrum from 300 to 1000 nm. MassAFRL Transmission Meeting. 15–16 June 2005. Available online: https://arxiv.org/pdf/astro-ph/0605029.pdf (accessed on 19 September 2024).
45. Thuillier, G.; Hersé, M.; Labs, D.; Foujols, T.; Peetermans, W.; Gillotay, D.; Simon, P.C.; Mandel, H. The solar spectral irradiance from 200 to 2400 nm as measured by the SOLSPEC spectrometer from the ATLAS and EURECA missions. *Sol. Phys.* **2003**, *214*, 1–22. [CrossRef]
46. Lei, N.; Xiong, X.; Guenther, B. Modeling the Detector Radiometric Gains of the Suomi NPP VIIRS Reflective Solar Bands. *IEEE Trans. Geosci. Remote Sens.* **2015**, *53*, 1565–1573. [CrossRef]
47. Iona, G.; Butler, J.; Guenther, B.; Johnson, E.; Kennedy, B.; Kent, C.; Lambeck, R.; Waluschka, E.; Xiong, X. VIIRS on-orbit optical anomaly: Investigation, analysis, root cause determination and lessons learned. *Proc. SPIE* **2012**, *8510*, 506–520. [CrossRef]
48. Li, Y.; Xiong, X.; McIntire, J.; Angal, A.; Gusev, S.; Chiang, K. Early Calibration and Performance Assessments of NOAA-20 VIIRS Thermal Emissive Bands. *IEEE Trans. Geosci. Remote Sens.* **2019**, *57*, 9242–9251. [CrossRef]
49. Mishra, N.; Helder, D.; Angal, A.; Choi, J.; Xiong, X. Absolute Calibration of Optical Satellite Sensors Using Libya 4 Pseudo Invariant Calibration Site. *Remote Sens.* **2014**, *6*, 1327–1346. [CrossRef]
50. Wu, A.; Xiong, X.; Mu, Q.; Angal, A.; Bhatt, R.; Shea, Y. Early Radiometric Assessment of NOAA-21 Visible Infrared Imaging Radiometer Suite Reflective Solar Bands Using Vicarious Techniques. *Remote Sens.* **2024**, *16*, 2528. [CrossRef]
51. David, R. Doelling, Daniel Morstad, Benjamin R. Scarino, Rajendra Bhatt, and Arun Gopalan. The Characterization of Deep Convective Clouds as an Invariant Calibration Target and as a Visible Calibration Technique. *IEEE Trans. Geosci. Remote Sens.* **2013**, *51*, 1147–1158. [CrossRef]
52. Lei, N.; Xiong, X.; Mu, Q.; Li, S.; Chang, T. Positional Dependence of SNPP VIIRS Solar Diffuser BRDF Change Factor. *IEEE Trans. Geosci. Remote Sens.* **2021**, *59*, 8056–8061. [CrossRef]
53. Lei, N.; Li, S.; Wilson, T.; Mu, Q.; Geng, X.; Twedt, K.; Angal, A.; Chang, T. NASA VCST N20 VIIRS VisNIR band L1B de-striping. *VCST Tech. Memo* **2023**, 2023_005.
54. Moeller, C.; Schwarting, T.; McCorkel, J.; Moyer, D.; McIntire, J. The JPSS-2 VIIRS version 2 at-launch relative spectral response characterization. *Proc. SPIE* **2019**, *11127*, 46–60. [CrossRef]
55. Twedt, K.; Lei, N.; Xiong, X. On-orbit noise characterization of the SNPP VIIRS reflective solar bands. *Proc. SPIE* **2017**, *10402*, 598–606. [CrossRef]

56. McIntire, J.; Moyer, D.; Chang, T.; Oudrari, H.; Xiong, X. Pre-Launch JPSS-2 VIIRS Response versus Scan Angle Characterization. *Remote Sens.* **2017**, *9*, 1300. [CrossRef]
57. Moyer, D.; McIntire, J.; Oudrari, H.; McCarthy, J.; Xiong, X.; De Luccia, F. JPSS-1 VIIRS Pre-Launch Response Versus Scan Angle Testing and Performance. *Remote Sens.* **2016**, *8*, 141. [CrossRef]